Active gust load alleviation of high-aspect ratio flexible wing aircraft

Ferrier, Yvonne L.; Nguyen, Nhan T.; Ting, Eric; Chaparro, Daniel; Wang, Xuerui; de Visser, Coen C.; Chu, Q. Ping

DOI
10.2514/6.2018-0620

Publication date
2018

Document Version
Final published version

Published in
AIAA Guidance, Navigation, and Control

AIAA SciTech Forum
8–12 January 2018, Kissimmee, Florida
2018 AIAA Guidance, Navigation, and Control Conference

10.2514/6.2018-0620

Active Gust Load Alleviation of High-Aspect Ratio Flexible Wing Aircraft

Y.L. Ferrier*

Delft University of Technology, Delft, The Netherlands

N.N. Nguyen†, E. Ting‡, D. Chaparro§

NASA Ames Research Center, Moffett Field, CA 94035

X. Wang ¶, C.C. de Visser‖, Q.P. Chu **

Delft University of Technology, Delft, The Netherlands

This paper presents a novel active gust load alleviation approach within a multi-objective flight control framework developed by NASA for a flexible wing aircraft. The aircraft model is based on the NASA Generic Transport Model (GTM). The wing structures incorporate an aerodynamic control surface known as the Variable Camber Continuous Trailing Edge Flap (VCCTEF). Previous work already showed the ability of the VCCTEF to perform aeroelastic mode suppression, drag minimization and maneuver load alleviation in a multi-objective flight control framework. In this paper, the multi-objective flight control framework is extended to include active gust load alleviation. A Linear-Quadratic Gaussian (LQG) controller is augmented with Model Reference Adaptive Control (MRAC) to provide active gust load alleviation. Disturbance estimation is done using an Extended State Observer (ESO) to support the design of the active gust load alleviation controller. The results demonstrate the potential of active gust load alleviation within a multi-objective flight control framework for a high-aspect ratio flexible wing aircraft embodied with the VCCTEF.

*MSc. student, Control and Simulation Section, Faculty of Aerospace Engineering, Delft University of Technology; Kluyverweg 1, 2629HS, Delft, The Netherlands. y.l.ferrier@tudelft.nl.

†Senior Research Scientist, Associate Fellow AIAA, Intelligent Systems Division, nhan.t.nguyen@nasa.gov

‡Engineer, Intelligent Systems Division, eric.b.ting@nasa.gov

§Engineer, Intelligent Systems Division, daniel.chaparro@nasa.gov

¶PhD Candidate, Control and Simulation Section, Faculty of Aerospace Engineering, Delft University of Technology; Kluyverweg 1, 2629HS, Delft, The Netherlands. X.Wang-6@tudelft.nl.

‖Assistant Professor, Control and Simulation Section, Faculty of Aerospace Engineering, Delft University of Technology; Kluyverweg 1, 2629HS, Delft, The Netherlands, c.c.devisser@tudelft.nl, AIAA member.

**Associate Professor, Control and Simulation Section, Faculty of Aerospace Engineering, Delft University of Technology; Kluyverweg 1, 2629HS, Delft, The Netherlands, Q.P.Chu@tudelft.nl, AIAA member.

I. Introduction

Formerly, aircraft were designed to provide safe load-carrying capacity by maintaining sufficient structural rigidity. The introduction of composite materials in commercial aircraft has disrupted the aviation industry by providing the same-load carrying capacity at lower weight. The weight reduction that results from the use of these composite airframes can translate into a fuel consumption advantage. This advantage has triggered aircraft manufacturers to design the airframes of their new-generation aircraft mostly out of composite materials. An example of a light-weight airframe design is the Boeing 787 Dreamliner aircraft, which uses at least 50% of composite materials in the airframe construction.

The composite wing structures provide the same load-carrying capacity, however exhibit less structural rigidity. The disadvantage of the increased flexibility of the wings is that, especially in combination with a high-aspect ratio, large aeroelastic deflections can occur that may result in adverse aerodynamics. The benefit of the weight reduction by using these composite materials could be annihilated by the increase in drag, and thus fuel consumption, due to the adverse aerodynamics. Performance Adaptive Aeroelastic Wing (PAAW) technology was developed under NASA Advanced Air Transport Technology project to address these challenges for future flexible wing transports. PAAW technology strives to find a multi-disciplinary solution that maximizes the aerodynamic performance of the future wing designs while also addressing the operational constraints that can mitigate the aerodynamic performance and flight safety. For high-aspect ratio flexible wing aircraft, the most important operational constraints are the reduced flutter margins, increased airframe responses to gust and maneuver loads, and degraded pilot handling and ride qualities.

A multi-objective flight control framework has been developed to simultaneously address the aerodynamic performance objective and the operational constraints.[1–3] This framework takes advantage of a multi-functional aerodynamic control surface called the Variable Camber Continuous Trailing Edge Flap (VCCTEF).[4–6]

The VCCTEF is a candidate PAAW concept that was initially proposed by NASA[1,4] and subsequently jointly developed by NASA and Boeing Research & Technology under the NASA Fixed Wing project in 2010. The VCCTEF, illustrated on the GTM in Fig. 1, provides active wing shaping control to improve the aerodynamic efficiency throughout a flight envelope. Initial studies indicate the ability of the VCCTEF to reduce drag for significant fuel savings[7,8] and the ability to provide flutter mode suppression and maneuver load alleviation in combination with drag cognizant control.[2,9]

This paper describes the formulation of an aeroservoelastic model of the GTM with the VCCTEF and the application of a multi-objective flight control framework focusing on gust load alleviation for an altitude-hold flight control mode in symmetric flight conditions.

The GTM aircraft model used in this study represents a general short-to-medium range commercial

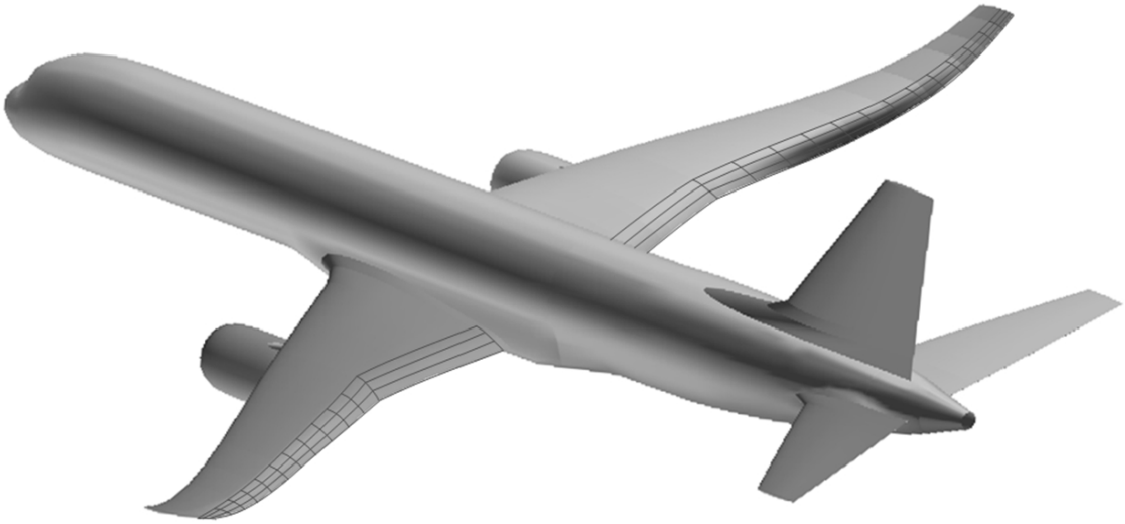

Figure 1. GTM with Variable Camber Continuous Trailing Edge Flap

passenger aircraft. The wing planform of the GTM incorporates the VCCTEF, illustrated in Fig. 2. The flap system consists of 16 individual spanwise sections which enable spanwise load tailoring. This lay-out provides the ability to control the wing twist shape in the spanwise direction. By changing the wing twist, and thus the spanwise loading, the aerodynamic performance can be improved for different flight conditions.

The spanwise flap sections are connected by an elastomer transition material, illustrated as black lines in between the spanwise flap sections as shown in Fig. 2. This transition material creates a continuous trailing edge flap when the flap sections are deflected. A continuous trailing edge flap has several advantages, such as improved aerodynamic efficiency and the mitigation of strong vortices by avoiding flap discontinuities.

The flap sections consist of three chordwise segments of equal chord length, illustrated in Fig. 3. These chordwise segments can be deflected individually to create camber surfaces for the desired aerodynamic performance. In this study the relative deflection of the chordwise segments is constrained to a circular-arc camber shape, which has a superior aerodynamic performance compared to other camber configurations,[10]

$$\begin{aligned} \delta_{i,1} &= \tfrac{1}{3}\delta_{i,3} \\ \delta_{i,2} &= \tfrac{2}{3}\delta_{i,3} \end{aligned} \tag{1}$$

This relation allows the control method to only regard the deflection of the outermost chordwise segment, $\delta_{i,3}$. The deflection angle of each chordwise segment is measured relative to the hinge and the undeflected trailing edge as shown in Fig. 3.

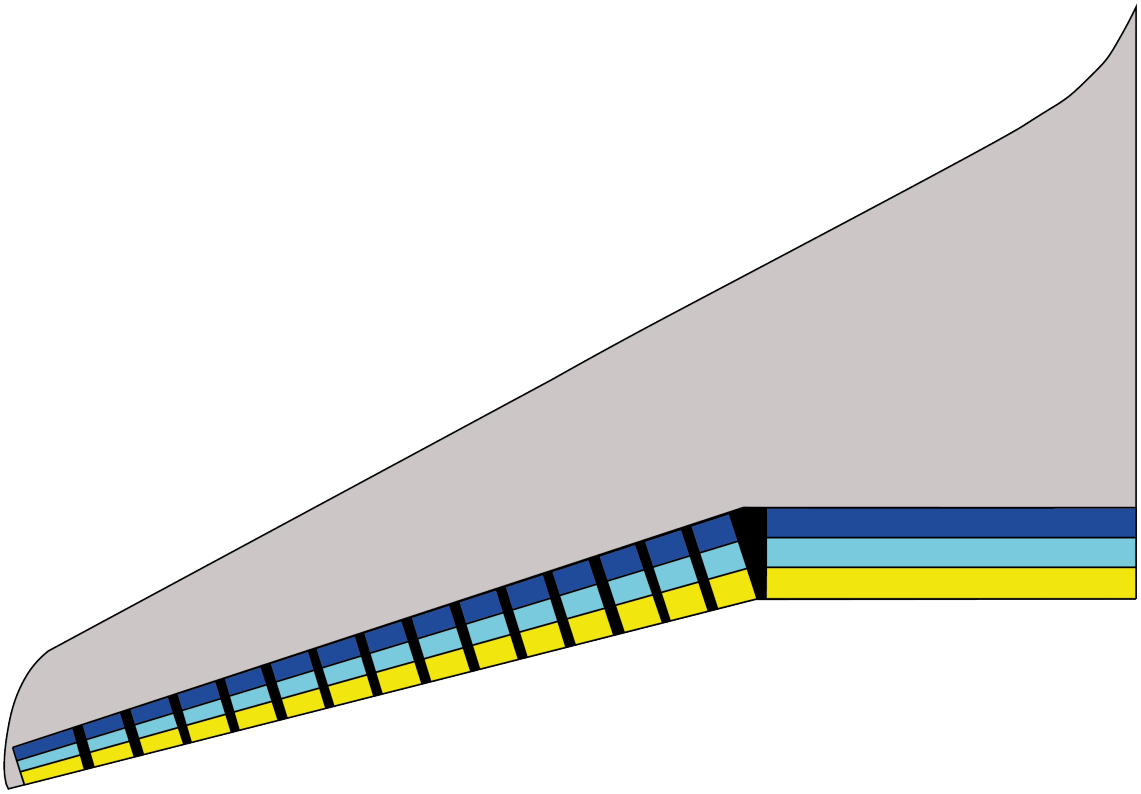

Figure 2. GTM Wing configured with VCCTEF

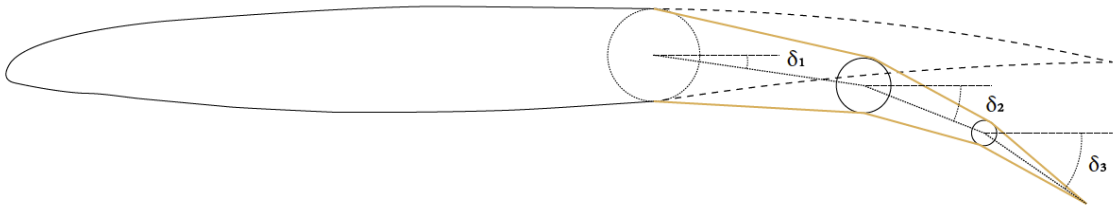

Figure 3. Three-Segment Variable Camber Continuous Trailing Edge Flap

II. Aeroservoelastic Model Formulation

For controller design and simulation purposes, an aeroservoelastic (ASE) model of a flexible wing aircraft equipped with the VCCTEF is developed by the Advanced Control and Evolvable Systems Group at NASA Ames Research Center. The ASE model includes the rigid aircraft flight dynamics, wing dynamic aeroelasticity, flight control actuator dynamics of the flap system, and servo-motor dynamics.[3,11,12]

In general, the rigid aircraft flight dynamic equation is expressed as[3]

$$M_r\dot{x}_r = Q_r\dot{x}_r + P_r x_r + D_r\delta_r + V_{rn}\ddot{q} + (T_{rn} + 0.5T_{rc})\,\dot{q} + \left[S_{rn} + 0.5S_{rc} + a_4\left(\frac{2V_\infty}{c}\right)T_{rc}\right]q + S_{rc}y + \left(\frac{2V_\infty}{c}\right)T_{rc}z + F_{rn}\ddot{\delta}_e + (E_{rn} + 0.5E_{rc})\,\dot{\delta} + \left[D_{rn} + 0.5D_{rc} + a_4\left(\frac{2V_\infty}{c}\right)E_{rc}\right]\delta + D_{rc}\nu + \left(\frac{2V_\infty}{c}\right)E_{rc}w \quad (2)$$

where x_r is the rigid aircraft state vector, q is the generalized displacement vector of the wing, y and z are the aerodynamic lag state vectors for the wing structural dynamics, δ_r is the rigid aircraft flight control surface deflection vector, δ is the VCCTEF deflection vector, ν and w are the aerodynamic lag state vectors for the VCCTEF actuator dynamics, the upper case variables are matrices, the subscript r denotes a rigid quantity, and the subscripts n and c signify non-circulatory and circulatory quantities according to the Theodorsen's theory.[9]

For symmetric flight conditions, the rigid aircraft state vector x_r includes the altitude h, airspeed V, angle of attack α, pitch rate q (not to be confused with the generalized displacement vector), and pitch angle θ. The rigid aircraft flight control surface deflection vector δ_r includes the thrust δ_T and elevator deflection δ_e.

The aerodynamic lag states account for the unsteady aerodynamic effect which is represented by the reduced frequency-dependent Theodorsen's function. The R.T. Jones approximation is used to convert the Theordorsen's function into a time-domain representation by the aerodynamic lag states.[12,13]

Using the finite-element formulation, the aeroelastic equation of the wing structure is discretized in generalized coordinates q (not to be confused with the pitch rate) as

$$(M_s + M_{an})\,\ddot{q} + (C_s + C_{an} + 0.5C_{ac})\,\dot{q} + \left[K_s + 0.5K_{ac} + a_4\left(\frac{2V_\infty}{c}\right)C_{ac}\right]q + K_{ac}y + \left(\frac{2V_\infty}{c}\right)C_{ac}z = Q_e\dot{x}_r + P_e x_r + F_{en}\ddot{\delta} + (E_{en} + 0.5E_{ec})\,\dot{\delta} + \left[D_{en} + 0.5D_{ec} + a_4\left(\frac{2V_\infty}{c}\right)E_{ec}\right]\delta + D_{ec}\nu + \left(\frac{2V_\infty}{c}\right)E_{ec}w \quad (3)$$

where the subscript s denotes a structural dynamic quantity, the subscript a denotes an aerodynamic quantity

due to the unsteady aerodynamic effect, and the subscript e denotes an aeroelastic quantity associated with the wing aeroelasticity.

The aerodynamic lag state equations for the wing structural dynamics obtained from the R.T. Jones approximation are

$$\ddot{y} + a_3\left(\frac{2V_\infty}{c}\right)\dot{y} + a_2\left(\frac{2V_\infty}{c}\right)^2 y = a_4\left(\frac{2V_\infty}{c}\right)\dot{q} + 0.5a_2\left(\frac{2V_\infty}{c}\right)^2 q \tag{4}$$

$$\ddot{z} + a_3\left(\frac{2V_\infty}{c}\right)\dot{z} + a_2\left(\frac{2V_\infty}{c}\right)^2 z = a_5\left(\frac{2V_\infty}{c}\right)\dot{q} + a_6\left(\frac{2V_\infty}{c}\right)^2 q \tag{5}$$

The actuator dynamic equation of the VCCTEF is expressed as

$$\begin{aligned} M_\delta\ddot{\delta} + C_\delta\dot{\delta} + K_\delta\delta = {} & Q_\delta\dot{x}_r + P_\delta x_r + V_{\delta n}\ddot{q} + \left(T_{\delta n} + 0.5T_{\delta c}\right)\dot{q} + \left[S_{\delta n} + 0.5S_{\delta c} + a_4\left(\frac{2V_\infty}{c}\right)T_{\delta c}\right]q \\ & + S_{\delta c}y + \left(\frac{2V_\infty}{c}\right)T_{\delta c}z + F_{\delta n}\ddot{\delta} + \left(E_{\delta n} + 0.5E_{\delta c}\right)\dot{\delta} + \left[D_{\delta n} + 0.5D_{\delta c} + a_4\left(\frac{2V_\infty}{c}\right)E_{\delta c}\right]\delta + D_{\delta c}\nu + \left(\frac{2V_\infty}{c}\right)E_{\delta c}w + \tau_\delta \end{aligned} \tag{6}$$

where τ_δ is the motor torque.

The aerodynamic lag state equations for the actuator dynamics are

$$\ddot{\nu} + a_3\left(\frac{2V_\infty}{c}\right)\dot{\nu} + a_2\left(\frac{2V_\infty}{c}\right)^2 \nu = a_4\left(\frac{2V_\infty}{c}\right)\dot{\delta} + 0.5a_2\left(\frac{2V_\infty}{c}\right)^2 \delta \tag{7}$$

$$\ddot{w} + a_3\left(\frac{2V_\infty}{c}\right)\dot{w} + a_2\left(\frac{2V_\infty}{c}\right)^2 w = a_5\left(\frac{2V_\infty}{c}\right)\dot{\delta} + 0.5a_6\left(\frac{2V_\infty}{c}\right)^2 \delta \tag{8}$$

The actuator dynamics of the rigid aircraft flight control are assumed to be a first-order model

$$\dot{\delta}_r = -\lambda\left(\delta_r - \delta_{rc}\right) \tag{9}$$

where $\lambda > 0$ is the actuator rate vector and δ_{rc} is the command vector of the rigid-body aircraft control.

The servo-motor dynamics for the VCCTEF are formed by a PID feedback control law

$$\dot{e} = \delta - \delta_c \tag{10}$$

$$\tau_\delta = k_p\left(\delta - \delta_c\right) + k_i e + k_d\dot{\delta} \tag{11}$$

where e is the integral error of the VCCTEF deflection command δ_c.

The fully coupled ASE flight dynamic model is given by Nguyen et al. (2017).[3] This ASE state-space model can be expressed as

$$\begin{bmatrix} M_{rr} & M_{re} & M_{r\delta} & M_{rs} \\ M_{er} & M_{ee} & M_{e\delta} & M_{es} \\ M_{\delta r} & M_{\delta e} & M_{\delta\delta} & M_{\delta s} \\ M_{sr} & M_{se} & M_{s\delta} & M_{ss} \end{bmatrix} \begin{bmatrix} \dot{x}_r \\ \dot{x}_e \\ \dot{x}_\delta \\ \dot{x}_s \end{bmatrix} = \begin{bmatrix} S_{rr} & S_{re} & S_{r\delta} & S_{rs} \\ S_{er} & S_{ee} & S_{e\delta} & S_{es} \\ S_{\delta r} & S_{\delta e} & S_{\delta\delta} & S_{\delta s} \\ S_{sr} & S_{se} & S_{s\delta} & S_{ss} \end{bmatrix} \begin{bmatrix} x_r \\ x_e \\ x_\delta \\ x_s \end{bmatrix} + \begin{bmatrix} T_r \\ T_e \\ T_\delta \\ T_s \end{bmatrix} u \tag{12}$$

where $x_r = \begin{bmatrix} h & u & \alpha & q & \theta \end{bmatrix}^T$, $x_e = \begin{bmatrix} q & y & z & \dot{q} & \dot{y} & \dot{z} \end{bmatrix}^T$, $x_\delta = \begin{bmatrix} \delta & \nu & w & \dot{\delta} & \dot{\nu} & \dot{w} \end{bmatrix}^T$, $x_s = \begin{bmatrix} \delta_r^T & e^T \end{bmatrix}^T$, and $u = \begin{bmatrix} \delta_{rc}^T & \delta_c^T \end{bmatrix}^T$. This dynamic model under gust excitation can be rewritten as

$$\dot{x} = Ax + Bu + w_g \tag{13}$$

where $x = \begin{bmatrix} x_r^T & x_e^T & x_\delta^T & x_s^T \end{bmatrix}^T$, w_g is the gust disturbance and

$$A = \begin{bmatrix} M_{rr} & M_{re} & M_{r\delta} & M_{rs} \\ M_{er} & M_{ee} & M_{e\delta} & M_{es} \\ M_{\delta r} & M_{\delta e} & M_{\delta\delta} & M_{\delta s} \\ M_{sr} & M_{se} & M_{s\delta} & M_{ss} \end{bmatrix}^{-1} \begin{bmatrix} S_{rr} & S_{re} & S_{r\delta} & S_{rs} \\ S_{er} & S_{ee} & S_{e\delta} & S_{es} \\ S_{\delta r} & S_{\delta e} & S_{\delta\delta} & S_{\delta s} \\ S_{sr} & S_{se} & S_{s\delta} & S_{ss} \end{bmatrix} \tag{14}$$

$$B = \begin{bmatrix} M_{rr} & M_{re} & M_{r\delta} & M_{rs} \\ M_{er} & M_{ee} & M_{e\delta} & M_{es} \\ M_{\delta r} & M_{\delta e} & M_{\delta\delta} & M_{\delta s} \\ M_{sr} & M_{se} & M_{s\delta} & M_{ss} \end{bmatrix}^{-1} \begin{bmatrix} T_r \\ T_e \\ T_\delta \\ T_s \end{bmatrix} \tag{15}$$

Four accelerometers are placed on the wing to observe the elastic states. Their output equations are computed as

$$\ddot{v} = \Phi\ddot{q} = \Phi E\dot{x}_e \tag{16}$$

where Φ is the matrix of eigenvectors and $E = \begin{bmatrix} 0 & 0 & 0 & I & 0 & 0 \end{bmatrix}$ such that $\ddot{q} = E\dot{x}_e$.

Then,

$$\ddot{v} = \Phi EG\left(Ax + Bu + w_g\right) \tag{17}$$

where $G = \begin{bmatrix} 0 & I & 0 & 0 \end{bmatrix}$ such that $\dot{x}_e = G\dot{x}$.

For a given acceleration location, then

$$\ddot{v}_c = F\ddot{v} = F\Phi EG\left(Ax + Bu + w_g\right) \tag{18}$$

where F is determined from the location of the acceleration measurement.

Let $y = \ddot{v}_c$ be the output, then

$$y = Cx + Du + Hw_g \tag{19}$$

where

$$C = F\Phi EGA \tag{20}$$

$$D = F\Phi EGB \tag{21}$$

$$H = F\Phi EG \tag{22}$$

In this study, the aircraft drag, wing root bending moment and vertical acceleration at the center of gravity are used in the multi-objective control formulation and to assess the controller performance. The aircraft drag is expressed as

$$C_D = C_{D_0} + \left(C_{L_0} + C_{L_{\dot{x}}}\dot{x} + C_{L_x}x + C_{L_u}u\right)^T K \left(C_{L_0} + C_{L_{\dot{x}}}\dot{x} + C_{L_x}x + C_{L_u}u\right) \tag{23}$$

The incremental drag is included in the optimal control cost function as a penalty for the drag minimization objective. From Eq.(23), the incremental drag is computed as

$$\Delta C_D = C_{D_x}x + C_{D_u}u + x^T C_{D_{x^2}}x + x^T C_{D_{xu}}u + u^T C_{D_{u^2}}u \tag{24}$$

The wing bending moment is expressed in general as

$$M_y = M_x x + M_u u + M_w w_g \tag{25}$$

where $M_w w_g$ is a bending moment component due to the gust disturbance.

The vertical acceleration at the aircraft center of gravity A_z is defined as

$$A_z = \frac{-Z}{m} \tag{26}$$

where Z is the downward vertical force and m is the aircraft mass. This definition can be expressed as

$$A_z = -V\dot{\alpha} - \dot{V}\alpha + qV + g\cos\theta \tag{27}$$

where V is the aircraft velocity, α is the angle of attack, q is the pitch rate, g is the local gravitational field of the Earth, and θ is the pitch angle. Because the term corresponding to the gravitational field is approximately constant ($g\cos\theta \approx g$), the incremental vertical acceleration of the aircraft center of gravity ΔA_z is used as a performance metric to evaluate the active gust load alleviation controller

$$\Delta A_z = -V\dot{\alpha} - \dot{V}\alpha + qV \tag{28}$$

The full-order coupled flight dynamic and ASE model includes a high number of elastic modes along with corresponding aerodynamic lag states. In this study, the full model has 198 elastic modes. Together with the rigid-body states, dynamic and aerodynamic lag states for the 16 VCCTEF elements and servo states this results in an ASE state-space model of 1307 states.

A reduced-order model is built for the convenience of a controller design. In general, an ASE state-space model contains rigid-body modes which usually have low frequencies and aeroelastic modes which are at higher frequencies than the rigid-body modes. In control design, it is sufficient to only consider the aeroelastic modes that are at the lower frequency range. This is because the high-frequency modes attenuate fast, and therefore have small response amplitudes. A reduced-order model is developed for control design purposes by only considering the low-frequency aeroelastic modes. The number of low-frequency aeroelastic modes is selected to ensure the flutter modes are captured. For this reduced-order model, the first lowest 10 frequency modes are retained.

III. Active Gust Load Alleviation in Multi-Objective Flight Control

A multi-objective flight control framework is designed to simultaneously address the operational constraints and the aerodynamic performance during the entire flight envelope. This is in contrast with conventional flight controllers of which the performance is only based on the pilot command-following ability. The introduction of the aerodynamic performance into the flight control framework allows the new controller to minimize the drag through adaptive aeroelastic wing shaping. This is done by adding a drag penalty into the control framework. The multi-objective flight control framework has both a pilot command-following objective and a drag reduction objective.[1–4]

Next to these two objectives, the stability of the aircraft is of utmost importance. The structural flexibility of the flexible wing aircraft can lead to degraded stability margins due to large aeroelastic deflections and interactions. The multi-objective flight control framework needs to contain an aeroelastic mode suppression objective to suppress the flutter or aeroelastic modes in order to meet the pilot handling quality requirements.

Furthermore, the increased airframe responses of flexible aircraft due to the gust and maneuver loads needs to be addressed. For flexible wing aircraft, gust disturbances and maneuvers can cause aeroelastic responses that may reduce the pilot handling and ride qualities. Gust load alleviation (GLA) can be provided by using either reactive feedback control or predictive feedforward control. The development of new sensor technologies such as light detection and ranging allows for predictive feedforward control methods. Currently, the advancement of these sensor technologies is still pending. Therefore this study uses reactive feedback control to design an active gust load alleviation approach. Likewise, the unwanted effects of maneuver loads can be suppressed by maneuver load alleviation.

In summary, the multi-objective flight control framework needs to harmoniously integrate the following objectives: 1) traditional pilot command-following control, 2) drag minimization, 3) aeroelastic mode suppression, and 4) gust and maneuver load alleviation. The integration of these objectives results in a complex control design that needs to take into account and compromise between competing objectives. The architecture of this control framework is illustrated in Fig. 4.[2] Next to these objectives a real-time drag minimization approach can be included in the control design.[8]

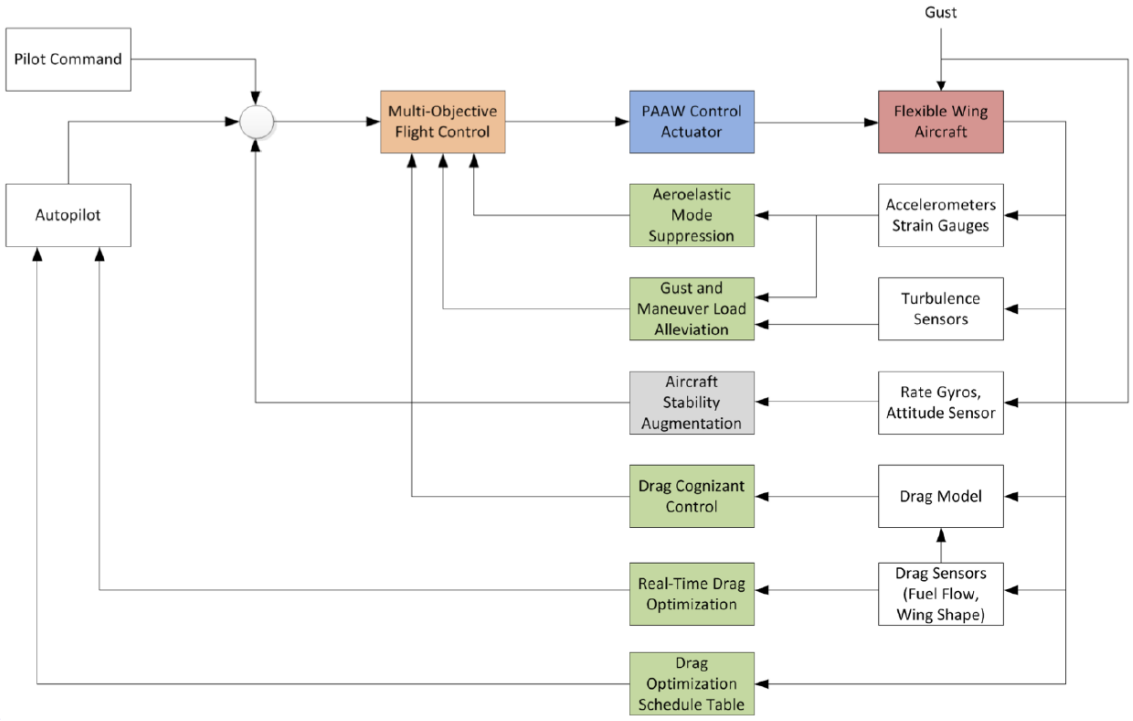

Figure 4. Multi-Objective Flight Control Architecture[2]

A. Controller Design

The flight controller is designed to provide an altitude-hold mode by following a flight path angle command. We define an integral error state of the flight path angle $x_a = \int_0^t \Delta\gamma d\tau$, where the error between the flight path angle and the command signal is expressed as

$$\Delta\gamma = \theta - \alpha - \gamma_c = A_a x_r - \gamma_c \tag{29}$$

where γ_c is the commanded flight path angle.

Now, let $x = \begin{bmatrix} x_r^T & x_e^T & x_\delta^T & x_s^T & x_a^T \end{bmatrix}^T$ and $u = \begin{bmatrix} \delta_{rc}^T & \delta_c^T \end{bmatrix}^T$, then the state-space system for the controller design is expressed as

$$\dot{x} = Ax + Bu + z + w_g \tag{30}$$

where

$$A = \begin{bmatrix} A_{rr} & A_{re} & A_{r\delta} & A_{rs} & 0 \\ A_{er} & A_{ee} & A_{e\delta} & A_{es} & 0 \\ A_{\delta r} & A_{\delta e} & A_{\delta\delta} & A_{\delta s} & 0 \\ A_{sr} & A_{se} & A_{s\delta} & A_{ss} & 0 \\ A_a & 0 & 0 & 0 & 0 \end{bmatrix}, \; B = \begin{bmatrix} B_{rr} & B_{re} \\ B_{er} & B_{ee} \\ B_{\delta r} & B_{\delta e} \\ B_{sr} & B_{se} \\ 0 & 0 \end{bmatrix} \; z = \begin{bmatrix} 0 \\ 0 \\ 0 \\ 0 \\ -\gamma_c \end{bmatrix} \tag{31}$$

The ASE state-space model of Eq.(30) can be written as

$$\dot{x}_r = A_{rr}x_r + A_{re}x_e + B_{rr}u_r + B_{re}u_e + z_r + w_r \tag{32}$$

$$\dot{x}_e = A_{er}x_r + A_{ee}x_e + B_{er}u_r + B_{ee}u_e + z_e + w_e \tag{33}$$

where x_r is the rigid-body state vector that includes the actuator state vector of the VCCTEF and the servo-motor state vector, x_e is the elastic state vector, u_r is the rigid aircraft control input vector, u_e is the VCCTEF control input vector, z_r is the command vector to the rigid aircraft state, z_e is the command vector to the elastic state, w_r is the disturbance to the rigid aircraft state, and w_e is the disturbance to the elastic state.

We formulate a multi-objective infinite time-horizon cost function as follows:

$$J = J_r + J_e \tag{34}$$

where

$$J_r = \lim_{t_f \to \infty} \frac{1}{2} \int_0^{t_f} \left[x_r^T Q_r x_r + u_r^T R_r u_r \right] dt \tag{35}$$

$$J_e = \lim_{t_f \to \infty} \frac{1}{2} \int_0^{t_f} \left[x_e^T Q_e x_e + u_e^T R_e u_e + q_D \Delta C_D \right] dt \tag{36}$$

The rigid aircraft controller u_r can be designed based on the cost function J_r to enable a rigid aircraft state $x_a = F x_r$ to track a command signal z. The VCCTEF controller u_e is designed based on the total cost function J to provide drag minimization and aeroelastic mode suppression.

B. Rigid Aircraft Control

A nominal rigid aircraft controller is designed to validate the performance of the multi-objective flight controller with active gust load alleviation. The design of the nominal rigid aircraft controller (NRC) is done by formulating the Hamiltonian function for the nominal rigid aircraft dynamics

$$H = \frac{1}{2} \left(x_r^T Q_r x_r + u_r R_r u_r \right) + \lambda^T \left(A_{rr} x_r + B_r u_r + z_r \right) \tag{37}$$

where λ is the adjoint variable.

The adjoint equation and optimal control are obtained as

$$\dot{\lambda} = -\frac{\partial H^T}{\partial x_r} = -Q_r x_r - A_{rr}^T \lambda \tag{38}$$

$$\frac{\partial H^T}{\partial u_r} = R_r u_r + B_r^T \lambda = 0 \Rightarrow u_r = -R_r B_r^T \lambda \tag{39}$$

subject to the transversality condition $\lambda(t_f) = 0$.

Let $\lambda = P x_r + S z_r$. Then,

$$\dot{P} x_r + P \dot{x}_r + \dot{S} z_r + S \dot{z}_r = -Q_r x_r - A_{rr}^T \left(P x_r + S z_r \right) \tag{40}$$

For the infinite time-horizon optimal control, $\dot{P} = 0$ and $\dot{S} = 0$. Therefore, we obtain the algebraic Ricatti equation

$$P A_{rr} + A_{rr}^T P - P B_r R_r^{-1} B_r^T P + Q_r = 0 \tag{41}$$

and

$$S = -\left(A_{rr}^T - PB_r R_r^{-1} B_r^T\right)^{-1} P \tag{42}$$

Then, the nominal rigid aircraft controller is given by

$$u_r = K_{x_r} x_r + K_z z_r \tag{43}$$

where

$$K_{x_r} = -R_r B_r^T P \tag{44}$$

$$K_{z_r} = -R_r B_r^T S \tag{45}$$

C. Multi-Objective Flight Control

The multi-objective flight controller is designed to include aeroelastic mode suppression and drag minimization.

We formulate the Hamiltonian of the total cost function J using the reduced-order model as

$$H = \frac{1}{2}\left(x^T Q x + u^T R u + q_D \Delta C_D\right) + \lambda^T \left(Ax + Bu + z\right) \tag{46}$$

Inserting Eq.(24) in the Hamiltonian gives

$$H = \frac{1}{2}x^T Q x + \frac{1}{2}u^T R u + \frac{1}{2}q_D \left(C_{D_x} x + C_{D_u} u + x^T C_{D_{x^2}} x + x^T C_{D_{xu}} u + u^T C_{D_{u^2}} u\right) + \lambda^T \left(Ax + Bu + z\right) \tag{47}$$

The adjoint equation and optimal control are obtained as

$$\dot{\lambda} = -\frac{\partial H^T}{\partial x} = -Qx - \frac{1}{2}q_D \left(C_{D_x}^T + 2C_{D_{x^2}}^T x + C_{D_{xu}}^T u\right) - A^T \lambda \tag{48}$$

$$\frac{\partial H^T}{\partial u} = Ru + \frac{1}{2}q_D \left(C_{D_u}^T + C_{D_{xu}}^T x + 2C_{D_{u^2}}^T u\right) + B^T \lambda = 0 \Rightarrow$$
$$u = -\left(R + q_D C_{D_{u^2}}^T\right)^{-1} \left(B^T \lambda + \frac{1}{2}q_D C_{D_u}^T + \frac{1}{2}q_D C_{D_{xu}}^T x\right) \tag{49}$$

We assume $\lambda = Wx + Vz + \lambda_0$. Then

$$\dot{W}x + W\dot{x} + \dot{V}z + V\dot{z} = -Qx - \frac{1}{2}q_D\left(C_{D_x}^T + 2C_{D_{x^2}}^T x + C_{D_{xu}}^T u\right) - A^T\left(Wx + Vz + \lambda_0\right) \tag{50}$$

Let γ_c be constant so that $\dot{\gamma}_c = 0$. Let $t_f \to \infty$, then the optimal solution approaches a steady-state solution. Therefore, $\dot{W}(t_f) = 0$ and $\dot{V}(t_f) = 0$. Then, separating terms yields the following expressions

$$W\bar{A} + \bar{A}^T W - WB\bar{R}^{-1}B^T W + \bar{Q} = 0 \tag{51}$$

$$V = -\left(\bar{A}^T - WB\bar{R}^{-1}B^T\right)^{-1} W \tag{52}$$

$$\lambda_0 = -\left(\bar{A}^T - WB\bar{R}^{-1}B^T\right)^{-1}\left(\frac{1}{2}q_D C_{D_x}\right) \tag{53}$$

where

$$\bar{R} = R + q_D C_{D_{u^2}}^T \tag{54}$$

$$\bar{A} = A - \frac{1}{2}q_D B\bar{R}^{-1}C_{D_{xu}}^T \tag{55}$$

$$\bar{Q} = Q + q_D C_{D_{x^2}}^T - \left(\frac{1}{2}q_D C_{D_{xu}}^T\right)^T \bar{R}^{-1}\left(\frac{1}{2}q_D C_{D_{xu}}^T\right) \tag{56}$$

Since $Q > 0$, $q_D > 0$, $C_{D_{x^2}} > 0$, and $C_{D_{xu}} > 0$ it follows that $\bar{Q} > 0$.

The multi-objective flight controller is expressed as

$$u = K_x x + K_z z + \Lambda_0 \tag{57}$$

where

$$K_x = -\bar{R}^{-1}\left(B^T W + \frac{1}{2}q_D C_{D_{xu}}^T\right) \tag{58}$$

$$K_z = -\bar{R}^{-1}B^T V \tag{59}$$

$$\Lambda_0 = -\bar{R}^{-1}\left(B^T\lambda_0 + \frac{1}{2}q_D C_{D_u}^T\right) \tag{60}$$

D. Disturbance Estimation using Extended State Observer

Active Gust Load Alleviation is a form of active disturbance rejection control, a control type that directly suppresses internal or external disturbances. This method requires measurement or estimation of the disturbances. Today, new sensor technologies, such as Light Detection and Ranging (LIDAR), are advancing rapidly and could be used for the prediction or measurement of turbulence. However, at the moment, the performance of these technologies are not yet reliable and sufficiently accurate. Therefore, this study proposes a disturbance estimation technique. The disturbance estimation is done using an Extended State Observer (ESO), introduced by Han in 1995.[14] The ESO is the extended version of a Luenberger observer. This observer is selected because of its low dependence on model accuracy and good robustness properties. The ESO estimates disturbances by extending the system of the observer states with disturbance states.

Consider a nonlinear system of order n:

$$\begin{aligned}
\dot{x}_1 &= f_1(x_1) + g_1(x_1)\,x_2 \\
\dot{x}_2 &= f_2(x_1, x_2) + g_2(x_1, x_2)\,x_3 \\
&\vdots \\
\dot{x}_n &= f_n(x_1, x_2, \ldots, x_n) + g_n(x_1, x_2, \ldots, x_n)\,u
\end{aligned} \tag{61}$$

An extended state observer of order $2n$, where the states from $\dot{x}_{n+1}$ forward are the extended states, for the system of Eq.(61) can be expressed as

$$\begin{aligned}
\dot{\hat{x}}_1 &= f_1(\hat{x}_1) + g_1(\hat{x}_1)\,\hat{x}_2 + \hat{x}_{n+1} - \beta_1^T e_1 \\
\dot{\hat{x}}_2 &= f_2(\hat{x}_1, \hat{x}_2) + g_2(\hat{x}_1, \hat{x}_2)\,\hat{x}_3 + \hat{x}_{n+2} - \beta_2^T e_2 \\
&\vdots \\
\dot{\hat{x}}_n &= f_n(\hat{x}_1, \hat{x}_2, \ldots, \hat{x}_n) + g_n(\hat{x}_1, \hat{x}_2\hat{x}_2, \ldots, \hat{x}_n)\,u + \hat{x}_{2n} - \beta_n^T e_n \\
\dot{\hat{x}}_{n+1} &= -\beta_{n+1}^T e_1 \\
\dot{\hat{x}}_{n+2} &= -\beta_{n+2}^T e_2 \\
&\vdots \\
\dot{\hat{x}}_{2n} &= -\beta_{2n}^T e_n
\end{aligned} \tag{62}$$

where e_i is the error between the estimated states and the system states

$$e_i = \hat{x}_i - x_i \tag{63}$$

and where β_i are the observer gains. The observer gains β_i can be chosen by pole placement of the error dynamics to provide stability.[15]

For this study, Eq.(62) can be rewritten as

$$\begin{aligned} \dot{\hat{x}}_{1\ldots n} &= A\hat{x}_{1\ldots n} + Bu + z_{1\ldots n} + \hat{w}_{g_{1\ldots n}} - \beta^T_{1\ldots n} e_{1\ldots n} \\ \dot{\hat{w}}_{g_{1\ldots n}} &= -\beta^T_{n+1\ldots 2n} e_{1\ldots n} \\ e_{1\ldots n} &= \hat{x}_{i\ldots n} - x_{i\ldots n} \end{aligned} \tag{64}$$

where $\hat{x}_{1\ldots n}$ are the observed states, $\hat{w}_g$ are the extended states and represent the estimates of the gust contribution w_g to the system states $x_{1\ldots n}$.

E. Active Gust Load Alleviation

Active Gust Load Alleviation uses Model Reference Adaptive Control (MRAC) to actively suppress the effect of turbulence. The multi-objective flight controller of Eq.(57) is the optimal baseline controller which is augmented with MRAC to actively cancel out the disturbance w_g.

The total control is expressed as

$$u\left(x, r, t\right) = u^*\left(x, r\right) + u_{ad}\left(t\right) \tag{65}$$

where u^* is the optimal baseline controller

$$u^* = K_x\hat{x} + K_z z + \Lambda_0 \tag{66}$$

and u_{ad} is the time-varying adaptive element.

The closed-loop dynamics of the reduced-order model are then obtained as

$$\dot{x} = \left(A + BK_x\right)x + BK_z z + \Lambda_0 + Bu_{ad} + z + w_g \tag{67}$$

The adaptive element u_{ad} is formulated according to MRAC principles to make the system states x track the states of a reference model x_{ref}. We define the reference model as

$$x_{ref} = A_{ref}x_{ref} + B_{ref}z + \Lambda_0 + z \tag{68}$$

where $A_{ref} = A + BKx$ is Hurwitz and $B_{ref} = BK_z$. The reference model represents the ideal closed-loop

behavior in the absence of turbulence.

The tracking error equation is obtained as

$$\dot{e} = \dot{x}_{ref} - \dot{x} = A_{ref}e - Bu_{ad} - w_g \tag{69}$$

If u_{ad} perfectly cancels out w_g, then the tracking error will tend to zero asymptotically, i.e., $e \to 0$ as $t_f \to \infty$. In practice, there will always be a small residual error. The adaptive signal is defined as

$$u_{ad} = \hat{K}_w \hat{w}_g \tag{70}$$

where $\hat{K}_w$ is the adaptive disturbance gain and $\hat{w}_g$ is the disturbance estimation. The definition of the adaptive signal as in Eq.(70) is inspired by optimal control theory. The adaptive disturbance gain $\hat{K}_w$ can be seen as an estimate of the optimal disturbance gain K_w. This optimal disturbance gain can be derived in theory using optimal control theory and the differential Lyapunov equation. See Appendix A for the derivation of the optimal disturbance gain.

This paper introduces the estimation of the optimal disturbance gain $\hat{K}_w$ as an alternative approach in order to avoid the use of the differential Lyapunov equation.

Inserting the definition of the adaptive signal of Eq.(70) into the tracking error equation of Eq.(69) gives

$$\dot{e} = \dot{x}_{ref} - \dot{x} = A_{ref}e - B\hat{K}_w \hat{w}_g - w_g \tag{71}$$

The adaptive disturbance gain $\hat{K}_w$ is computed by the direct MRAC update law

$$\dot{\hat{K}}_w^T = \Gamma \hat{w}_g e^T PB \tag{72}$$

where Γ is the MRAC gain matrix and P is the solution to the algebraic Lyapunov equation

$$PA_{ref} + A_{ref}^T P = -Q \tag{73}$$

with $Q > 0$.[16] The stability of the MRAC update law can be shown with Lyapunov stability theorem.

Proof: Choose a Lyapunov candidate function

$$V = e^T Pe + \text{trace}\left(\hat{K}_w \Gamma^{-1} \hat{K}_w^T\right) \tag{74}$$

Then, $\dot{V}$ is evaluated as

$$\dot{V} = -e^T Q e + 2e^T P\left(-B\hat{K}_w\hat{w}_g - w_g\right) + 2\text{trace}\left(\hat{K}_w\Gamma^{-1}\dot{\hat{K}}_w^T\right)$$
$$= -e^T Q e - 2\text{trace}\left(\hat{K}_w\hat{w}_g e^T PB\right) - 2e^T P w_g + 2\text{trace}\left(\hat{K}_w\Gamma^{-1}\dot{\hat{K}}_w^T\right)$$
$$= -e^T Q e - 2e^T P w_g + 2\text{trace}\left(\hat{K}_w\left(-\hat{w}_g e^T PB + \Gamma^{-1}\dot{\hat{K}}_w^T\right)\right)$$

The definition of the update law becomes

$$-\hat{w}_g e^T PB + \Gamma^{-1}\dot{\hat{K}}_w^T = 0 \Rightarrow \dot{\hat{K}}_w^T = \Gamma\hat{w}_g e^T PB \tag{75}$$

Therefore $\dot{V}$ becomes

$$\dot{V} = -e^T Q e - 2e^T P w_g \leq -\lambda_{min}(Q)\|e\|^2 + 2\lambda_{max}(P)\|e\|\|w_g\| \tag{76}$$

Thus, $\dot{V} \leq 0$ implies

$$\|e\| \geq \frac{2\lambda_{max}(P)\|w_g\|}{\lambda_{min}(Q)} \tag{77}$$

This implies e is bounded as $t \to \infty$. One cannot assume that $e \to 0$ because w_g is unknown.

The total control includes the linear-quadratic optimal control and the active gust load alleviation control

$$u = K_x x + K_z z + \Lambda_0 + \hat{K}_w\hat{w}_g \tag{78}$$

F. VCCTEF Virtual Control Variables

The elastomer transition material between the spanwise flap sections of the VCCTEF limits the relative motion between these sections. The elastomer transition material has certain displacement and rate limits, and consequently the flap sections are also constrained by relative displacement and rate limits. The relative constraints between the spanwise flap sections need to be included in the control design.

The constraints can be expressed as

$$|\delta_{i+1} - \delta_i| \leq \dot{\delta} \tag{79}$$

$$\left|\dot{\delta}_{i+1} - \dot{\delta}_i\right| \leq \Delta\dot{\delta} \tag{80}$$

where $i = 1, 2, \ldots, m$ is the index of the flap section and m is the total number of spanwise flap sections per

wing.

The displacement constraint between each adjacent spanwise flap section for the VCCTEF is assumed to be 2°. The rate constraint is not defined and therefore not considered in this study.

The relative deflection limit is addressed in the control design by implementing a virtual control concept.[1] The deflections of the flap sections are constrained to a mathematical shape function. The actual flap deflections can now be described by a set of virtual control variables. In this study, the spanwise flap sections are constrained to a shape function described by a cubic Chebyshev polynomial of the first kind as[20]

$$\delta_i = c_0 + c_1 k + c_2 \left(2k^2 - 1\right) + c_3 \left(4k^3 - 3k\right) \tag{81}$$

where $k = \frac{i-1}{n-1}$, $i = 1, 2, \ldots, n$, $n = 16$, and $c_j\left(t\right), j = 0, 1, 2, 3$ are the virtual control variables.

The control design determines the commands for the virtual control variables with the implementation of this shape function. Since the shape function in Eq.(81) is linear with respect to the virtual control variables, a transformation matrix can be constructed that relates the physical control variables to the virtual control variables with the use of partial derivation.

IV. Simulations

Simulations are conducted to assess the performance of the active gust load alleviation control method in combination with the multi-objective flight controller. The simulations use the coupled ASE longitudinal dynamic model of the flexible wing GTM with VCCTEF as described in Section II. The wing stiffness is reduced by 50% from the baseline stiffness. The model has five rigid aircraft states in the longitudinal direction, 198 aeroelastic modes with two elastic states and four aerodynamic lag states per mode, two rigid aircraft flight control inputs; namely the engine throttle and elevator each with one actuator state, and 16 VCCTEF inputs to the outermost chordwise flap segments with two actuator states and four aerodynamic lag states per flap segment. Thus, the model has a total of 1307 states and 18 control variables. The model includes an aerodynamic model that computes the aircraft drag coefficient according to Eq.(23), a structural model that computes the wing root bending moment from Eq.(25), as well as accelerometer models that compute the vertical accelerations of the aeroelastic modes at the wing from Eq.(19) and the aircraft center of gravity from Eq.(27).

The controller is built using the reduced-order model that contains the first 10 aeroelastic modes. This reduced-order model has 179 states.

A flight path angle control is designed according to Eq.(30). The flight path angle command γ_c stays equal to 0, resulting in the objective of the baseline controller to stay at normal cruise conditions in the

presence of turbulence. Cruise conditions for the GTM with VCCTEF are at Mach 0.797 at an altitude of 36,000 ft.

The optimal baseline controller has the cost weighting matrix $Q\left(x_r, x_e, x_\delta, x_s, x_a\right) = diag(100, 50, 1 \times 10^{-10}, 1 \times 10^{-10}, 1 \times 10^{6})$ and the control weighting matrix is selected as $R = 1 \times 10^4 I$. As can be seen from the cost weighting matrix, the aeroelastic mode suppression uses as weighting matrix $Q_e = 50$. The drag minimization uses a weighting coefficient $q_D = 5 \times 10^4$. The nominal rigid controller has the same control weighting matrix and cost weighting matrix $Q\left(x_r, x_\delta, x_s, x_a\right) = diag(100, 1 \times 10^{-10}, 1 \times 10^{-10}, 1 \times 10^{6})$.

The disturbance estimation is done using the ESO described in Eq.(64). The observer gains are selected as $\beta_i = 100$ for the rigid-body states x_r, aeroelastic states derivatives $\dot{q}$, and the VCCTEF states derivatives $\dot{\delta}$. Since the other states are not directly affected by the turbulence, their observer gains are kept to 0.

The MRAC update law for the adaptive disturbance gain of the active gust load alleviation control in Eq.(72) is calculated with the MRAC rates of adaptation $\Gamma(x_r) = 1 \times 10^3, \Gamma(x_e) = \Gamma(x_\delta) = 1 \times 10^{-2}$ and weight matrix $Q\left(x_r, x_e, x_\delta, x_s, x_a\right) = diag(5 \times 10^1, 1 \times 10^1, 1 \times 10^{-1}, 0, 0)$.

The simulations consider a 1-dimensional severe von Kármán turbulence model with a turbulence intensity σ of 4.5 and a characteristic length L of $1750ft$.

A. Aeroelastic State Estimation

The multi-objective flight controller with active gust load alleviation is a feedback control design. This means that the control design needs information about the states. In this study, it is assumed that the rigid-body states x_r, VCCTEF states x_δ, and servo-motor states x_s can be measured. The aeroelastic state vector x_e cannot be measured and therefore needs to be estimated with an observer design.

The inclusion of an observer in the optimal control framework of the multi-objective flight controller transforms the Linear-Quadratic Regulator (LQR) control to Linear-Quadratic Gaussian (LQG) control. The state observer is designed using the Kalman filter optimal estimation method.

The state observer uses the measurements from four accelerometers that are placed in pairs at mid-span and near the wing tip of each wing. The accelerometer pairs are located forward and aft of the elastic axis at the same spanwise location, illustrated by the red dots in Fig.5. This relative positioning of the accelerometer pairs with respect to the elastic axis allows the measurement of both the vertical and angular acceleration of the wing section.

The accelerometer measurements need to be filtered before they can be used in the Kalman filter estimation. This is because of two reasons: 1) measurement noise needs to diminish, and 2) the effect of the high-frequency modes that are removed in the reduced-order model needs to be attenuated. Otherwise, these high-frequency modes can significantly affect the accelerometer output, but this effect is not taken into

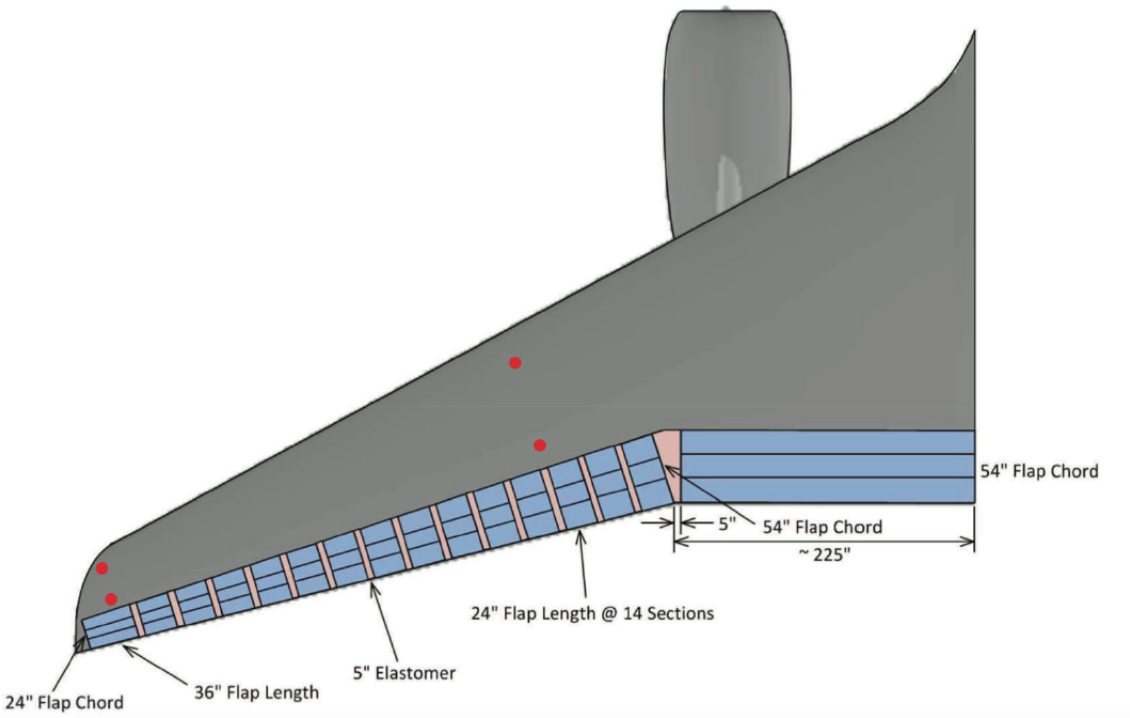

Figure 5. Accelerometer Locations

account in the predicted output of the Kalman filter. The disparity between the measured and predicted output can negatively influence the state estimation. A low-pass filter provides a solution to both problems. The cut-off frequency of the filter should be selected based on the maximum frequency of the aeroelastic modes in the reduced-order model. A Bessel filter is selected since this filter has a limited phase shift and therefore a smaller delay with respect to the accelerometer measurements.[2]

In this simulation study, the outputs of the four accelerometers are modeled by Eq.(19). The Kalman filter estimates the aeroelastic states with

$$\dot{\hat{x}}_e = A_{er}x_r + A_{ee}\hat{x}_e + A_{e\delta}x_\delta + A_{es}x_s + B_e u + z_e + L\left(y_K - \hat{y}\right) \tag{82}$$

where L is the optimal Kalman filter gain and $\hat{y}$ is the estimated output as

$$\hat{y} = C\begin{bmatrix} x_r^T & \hat{x}_e^T & x_\delta^T & x_s^T & x_a^T \end{bmatrix}^T + Du \tag{83}$$

and y_K is the filtered accelerometer output given by

$$y_K = F(s)\left(y + v\right) \tag{84}$$

where $F(s)$ is the transfer function of the Bessel filter and v is the measurement noise. The measurement

noise is modeled as white noise.

By implementing the state estimates in the controller design of Eq.(78), the multi-objective flight controller with active gust load alleviation becomes

$$u = K_x\hat{x} + K_z z + \Lambda_0 + \hat{K}_w\hat{w}_g \tag{85}$$

where $x = \begin{bmatrix} x_r^T & \hat{x}_e^T & x_\delta^T & x_s^T & x_a^T \end{bmatrix}^T$.

B. Performance Metrics for Gust Load Alleviation

The goal of the simulations is to assess the performance of the active gust load alleviation control method. Several performance metrics have been used in previous research on gust load alleviation to analyze the controller performance. In this study, five performance metrics will be analyzed

1. The sum of the Euclidean norm of the rigid-body states

$$\sum_{i=1}^{m_r} \|x_r - x_{ref,r}\| = \sum_{i=1}^{m_r} \left(\sum_{j=1}^{n} |x_{r,ij}|^2 \right)^{1/2} \tag{86}$$

where n is the number of samples and m_r is the number of rigid-states.

2. The sum of the Euclidean norm of the aeroelastic states

$$\sum_{i=1}^{m_e} \|x_e - x_{ref,e}\| = \sum_{i=1}^{m_e} \left(\sum_{j=1}^{n} |x_{e,ij}|^2 \right)^{1/2} \tag{87}$$

where m_e is the number of elastic states.

3. The Euclidean norm of the flight path angle γ

$$\|\gamma - \gamma_{ref}\| = \left(\sum_{j=1}^{n} |\gamma_j|^2 \right)^{1/2} \tag{88}$$

4. The root-mean-square incremental vertical acceleration at the center of gravity of the aircraft

$$A_{z,rms} = \sqrt{\frac{1}{n} \sum_{i=1}^{n} \Delta A_{z,i}^2} \tag{89}$$

5. The root-mean-square bending moment at the wing root

$$M_{y,rms} = \sqrt{\frac{1}{n}\sum_{i=1}^{n} M_{y,i}^2} \tag{90}$$

In previous research,[21–24] the wing root bending moment M_y and the rigid-body x_r and elastic state x_e responses have been selected as the main performance metrics to consider. Consequently, the performance metrics relating to these variables (1, 2, and 5) will be considered to be of most importance.

Furthermore, the drag minimization control feature is also analyzed. The incremental drag is calculated according to Eq.(24).

C. Simulation Results

This section contains the results of the simulations for the flexible wing GTM aircraft in symmetric cruise conditions subjected to severe von Kármán turbulence. The performance of seven different controllers is analyzed and compared:

1. Nominal Rigid Controller (NRC)
2. Linear-Quadratic Regulator Control (LQR)
3. Linear-Quadratic Regulator Control with Drag Minimization (LQR + DM)
4. Linear-Quadratic Regulator Control with Drag Minimization and Active Gust Load Alleviation (LQR + DM + GLA)
5. Linear-Quadratic Gaussian Control (LQG)
6. Linear-Quadratic Gaussian Control with Drag Minimization (LQG + DM)
7. Linear-Quadratic Gaussian Control with Drag Minimization and Active Gust Load Alleviation (LQG + DM + GLA)

The difference between LQR and LQG is that the LQR controller assumes that all the states can be measured, while the LQG controller needs the Kalman filter estimation of the aeroelastic states. Both the LQR and LQG controller include the aeroelastic mode suppression objective ($Q_e = 50$). Drag minimization is added to the controller by switching the drag weighting coefficient q_D from 0 to 5×10^4.

Tables 1 and 2 show the performance metric results of the flight dynamic, structural and aerodynamic responses. In these tables both the LQR and LQG simulations are shown. The LQG simulations represent the most realistic scenario, in which the aeroelastic states cannot be measured but need to be estimated with

the use of a Kalman filter. This state estimation introduces errors in the control method. For this reason, the LQR simulations are also shown. The LQR simulations show the performance of the aeroelastic mode suppression, drag minimization, and active gust load alleviation without the interference of state estimation errors.

	$\sum \|x_r - x_{ref,r}\|$	%	$\sum \|x_e - x_{ref,e}\|$	%	$\|\gamma - \gamma_{ref}\|$	%
NRC	0.395	0	20.355	0	1.169	0
LQR	0.368	-7	11.735	-42	1.521	30
LQR + DM	0.289	-27	9.755	-52	0.876	-25
LQR + DM + GLA	0.114	-71	14.078	-80	0.665	-43
LQG	0.461	17	17.886	-12	0.366	-69
LQG + DM	0.321	-19	11.732	-42	0.604	-48
LQG + DM + GLA	0.175	-56	6.078	-70	0.724	-38

Table 1. Performance Metrics Results: Flight Dynamic Responses

First of all, the aeroelastic mode suppression is noticeable by considering the sum of the Euclidean norm of the aeroelastic states $\sum \|x_e - x_{ref,e}\|$. The LQR and LQG controllers significantly suppress the aeroelastic responses. Furthermore, the Euclidean norms of the rigid-body states $\sum \|x_r - x_{ref,r}\|$ and aeroelastic states $\sum \|x_e - x_{ref,e}\|$ show the ability of the active gust load alleviation control to significantly counteract the effects of the turbulence. The drag minimization objective also suppresses the rigid-body and aeroelastic states. The performance metric related to the flight path angle $\|\gamma - \gamma_{ref}\|$ shows an increase in performance for the LQR controllers when adding drag minimization and active gust load alleviation. The LQG controller, however, shows the opposite effect with respect to this flight path angle performance metric. The contrary results could be caused by errors in the aeroelastic state estimation.

	$A_{z,rms}$ $[ft/s^2]$	%	$M_{y,rms}$ $[ft-lb]$	%	ΔC_D [dragcount]	%
NRC	0.482	0	63598	0	18	0
LQR	0.296	-39	26352	-59	23	28
LQR + DM	0.241	-50	15374	-76	21	17
LQR + DM + GLA	0.268	-44	10584	-83	18	0
LQG	0.187	-61	46289	-27	21	17
LQG + DM	0.235	-51	29781	-53	19	6
LQG + DM + GLA	0.269	-44	10533	-83	19	6

Table 2. Performance Metrics Results: Structural and Aerodynamic Responses

The results in Table 2 show the ability of active gust load alleviation to significantly decrease the root-mean-square of the wing root bending moment $M_{y,rms}$. As mentioned earlier, the wing root bending moment is a main criterion in the analysis of gust load alleviation controls. The vertical acceleration of the center of gravity $A_{z,rms}$ decreases when including aeroelastic mode suppression, but does not show a coherent relation with the controller type. The incremental drag ΔC_D is lowest for the nominal rigid controller. However, the

effect of drag minimization control is certainly noticeable when comparing the LQR and LQG controllers with the LQR and LQG controllers with drag minimization.

Figure 6 shows the incremental rigid-body response of the aircraft to the severe von Kármán turbulence. The plots compare the responses of the nominal rigid controller, the LQG controller with aeroelastic mode suppression, the LQG controller with aeroelastic mode suppression and drag minimization and the LQG controller with aeroelastic mode suppression, drag minimization, and active gust load alleviation. The angle of attack $\Delta\alpha$ and pitch angle $\Delta\theta$ illustrate the improvements gained by including drag minimization and the significant improvement when including active gust load alleviation. The pitch rate Δq shows a clear improvement of all the LQG controllers with respect to the nominal rigid controller. Furthermore, active gust load alleviation shows the largest improvement in suppressing the response of the pitch rate. The flight path angle γ response benefits the most from aeroelastic mode suppression, and all LQG controllers perform better than the nominal rigid controller.

Figure 7 shows the response of the first three aeroelastic modes. The effect of active gust load alleviation is clearly visible. The LQG controller with mode suppression, drag minimization, and active gust load alleviation performs best in suppressing the aeroelastic states.

Figure 8 shows the control surface deflections of the elevator and the VCCTEF. The VCCTEF sections are numbered from 1 at the wing root to 16 at the wing tip. The elevator deflections are well within the standard elevator deflection limit of 25° and the deflection rates are well-behaved. The VCCTEF deflections are illustrated separately for the four different controllers. For all control methods the VCCTEF deflections are well-behaved and within the deflection limit of 20°. Furthermore, the deflection limit constraint of 2° between each adjacent flap section is obeyed. The inclusion of the aeroelastic mode suppression objective results in higher control surface deflections.

Figure 9 shows the wing root bending moment response ΔM_y, vertical acceleration at the center of gravity response ΔA_z, and the incremental drag response ΔC_D. The wing root bending moment is significantly decreased with the use of active gust load alleviation. The vertical acceleration at the center of gravity is mainly suppressed by the aeroelastic mode suppression objective. The incremental drag is lowest for the nominal rigid controller. However, the drag minimization objective decreases the incremental drag with respect to the LQG controller.

Figure 10 shows the results of the ESO disturbance estimation. In this figure, the estimations of the disturbance to the angle of attack w_{g_α} and the disturbance to the first aeroelastic mode $w_{g_{q1}}$ are compared for the LQR and LQG simulations. First of all, for both the LQR and LQG simulations the estimation of the disturbance to the angle of attack is reasonably accurate. Secondly, the estimation of the disturbance to the first aeroelastic mode is again accurate for the LQR simulation, but far off for the LQG simulation.

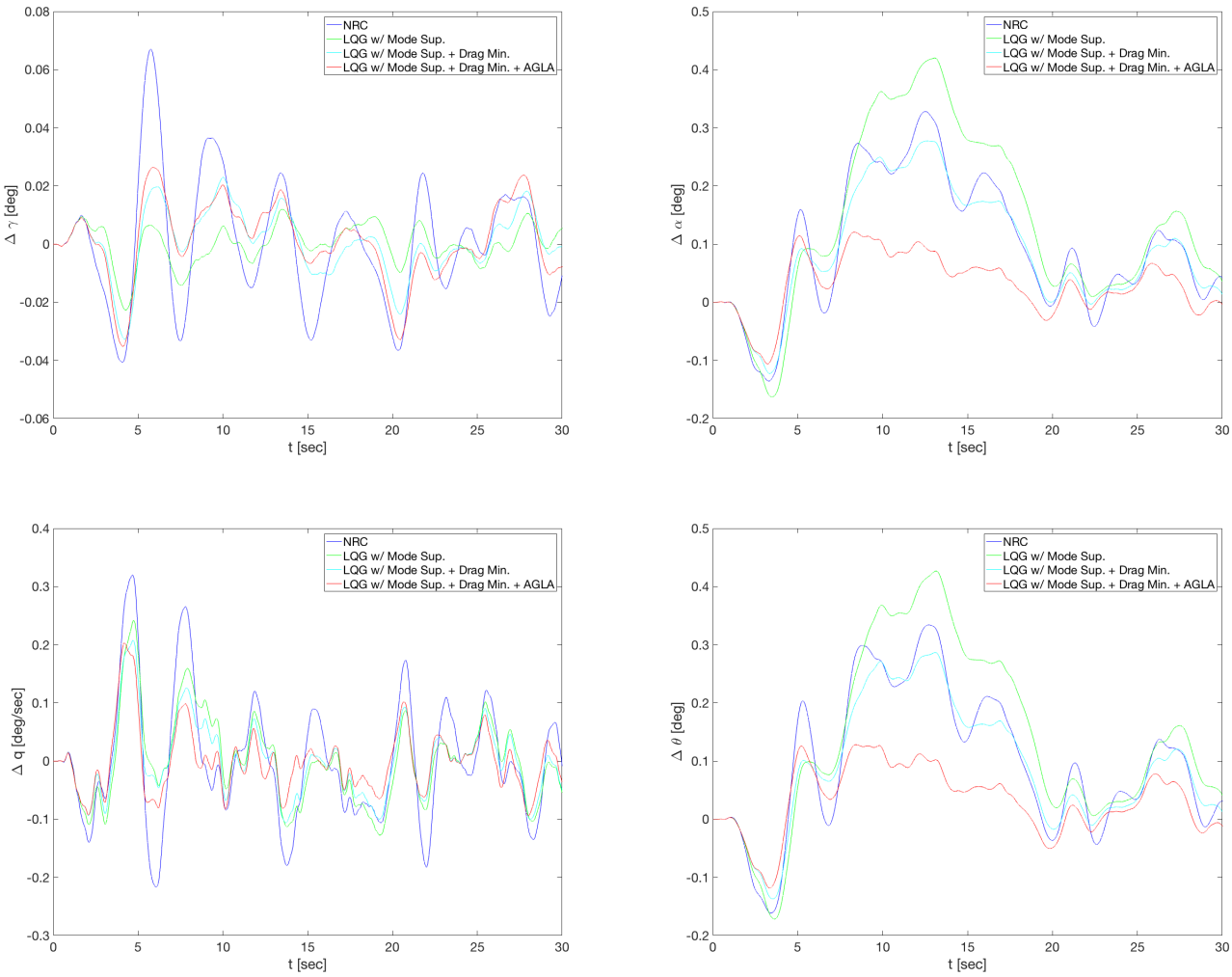

Figure 6. Rigid Aircraft Response to Multi-Objective Flight Control with Mode Suppression, Drag Minimization and Active Gust Load Alleviation

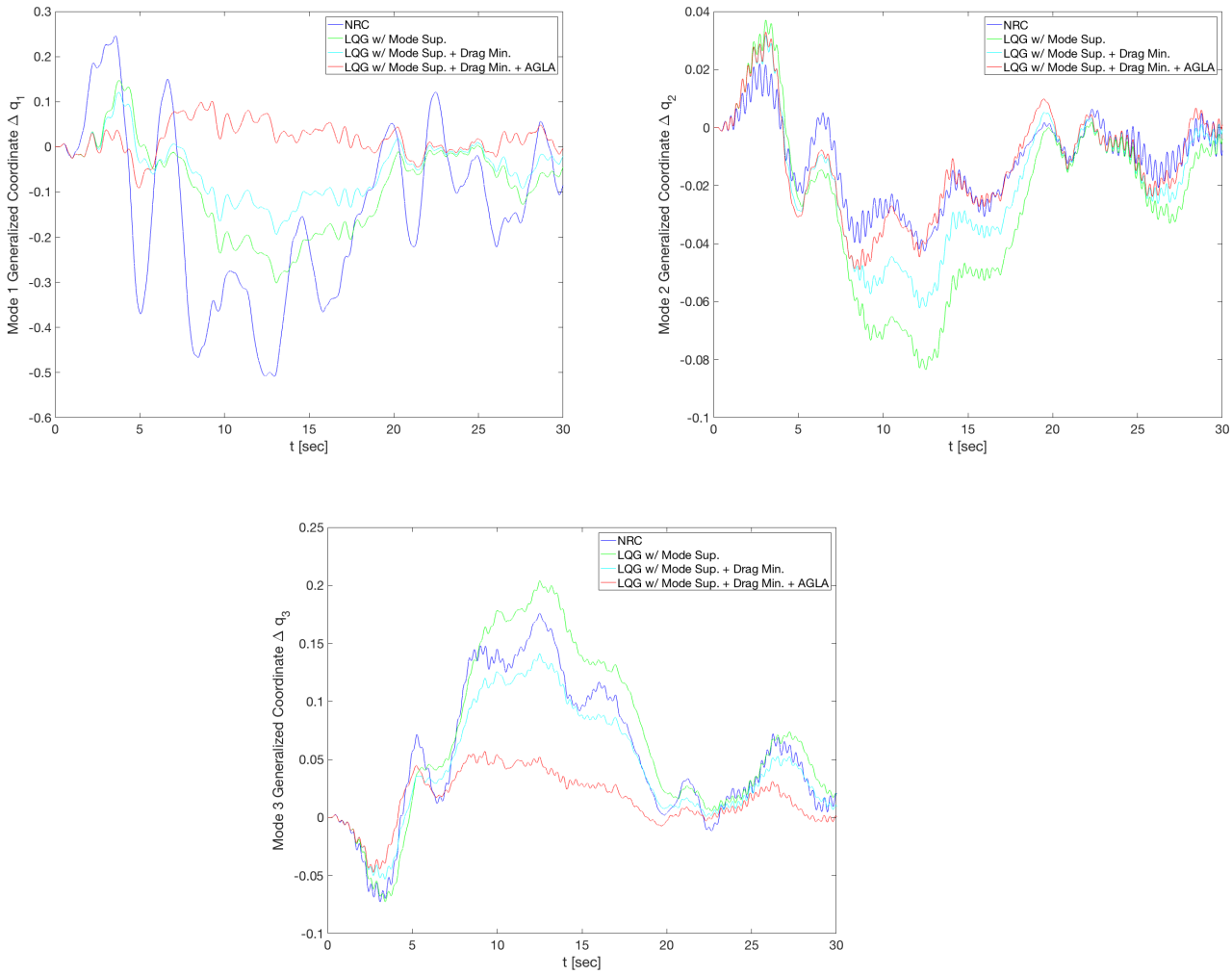

Figure 7. Elastic Response to Multi-Objective Flight Control with Mode Suppression, Drag Minimization and Active Gust Load Alleviation

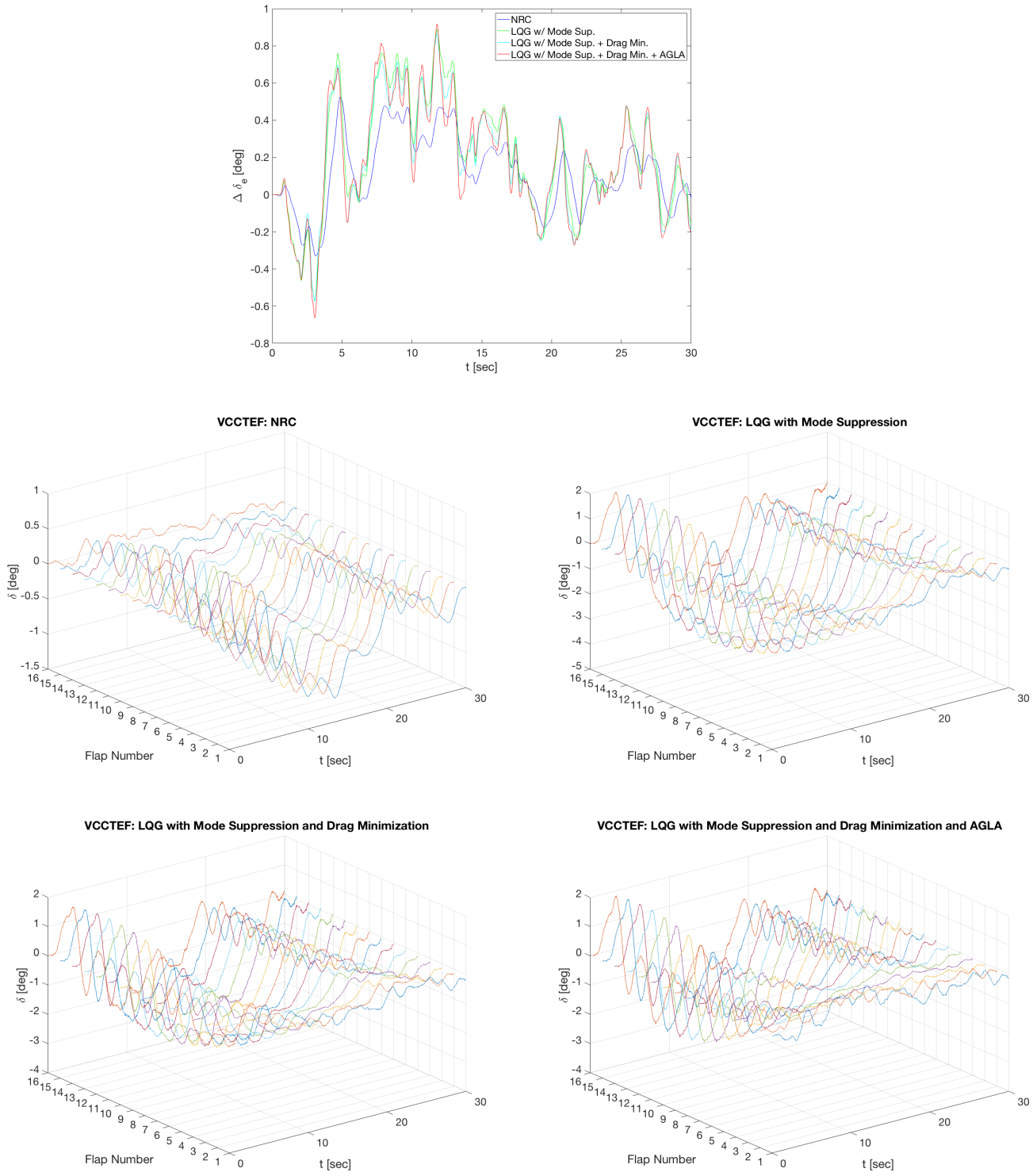

Figure 8. Control Surface Deflections for Multi-Objective Flight Control with Mode Suppression and Drag Minimization

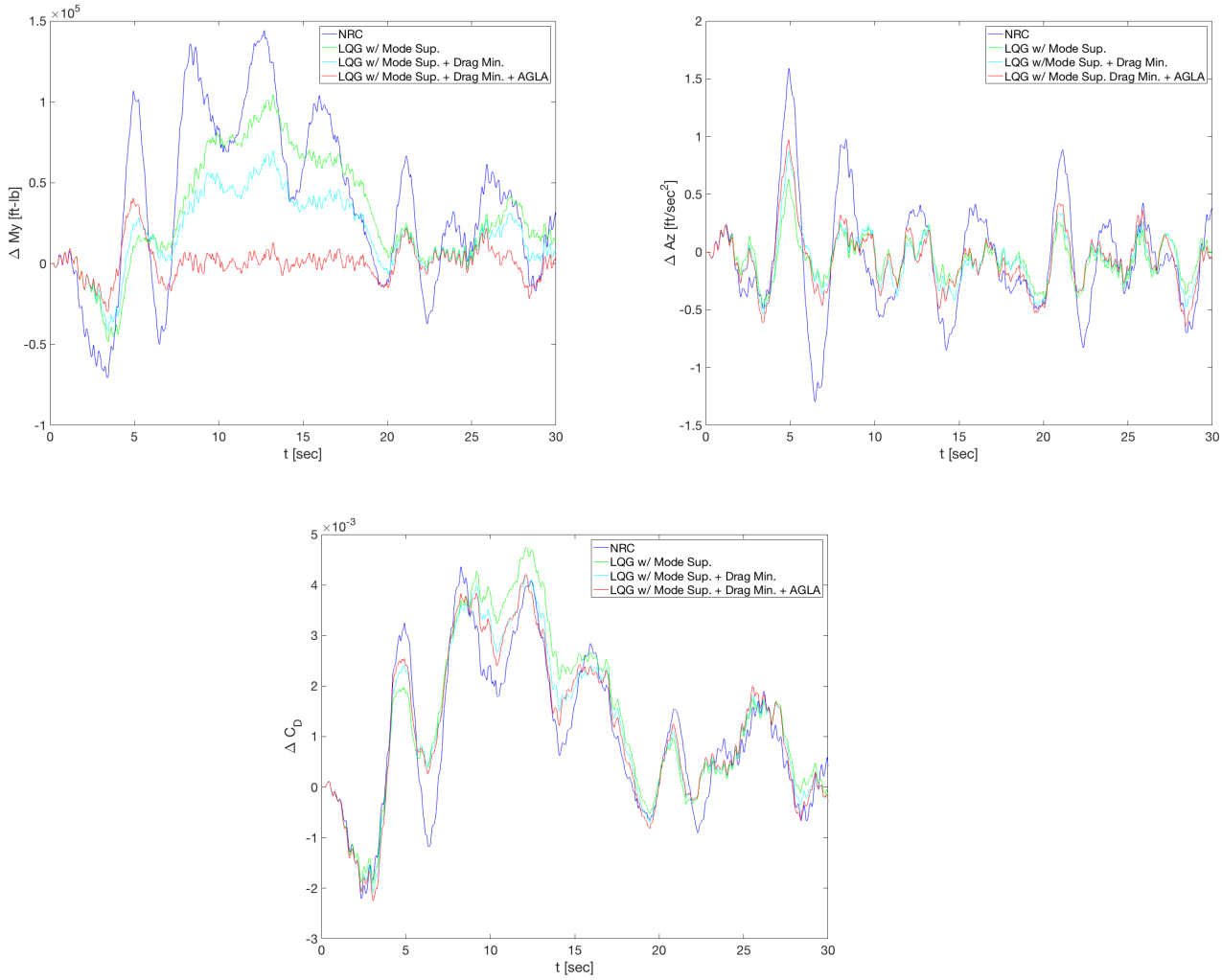

Figure 9. Performance Response to Multi-Objective Flight Control with Mode Suppression, Drag Minimization and Active Gust Load Alleviation

This means that the errors between the actual and estimated aeroelastic states significantly impact the ESO estimation of the disturbances related to the aeroelastic states. Both the disturbance estimations for the LQR and LQG controllers show a phase lag with respect to the real disturbance. This lag decreases the performance of the controllers.

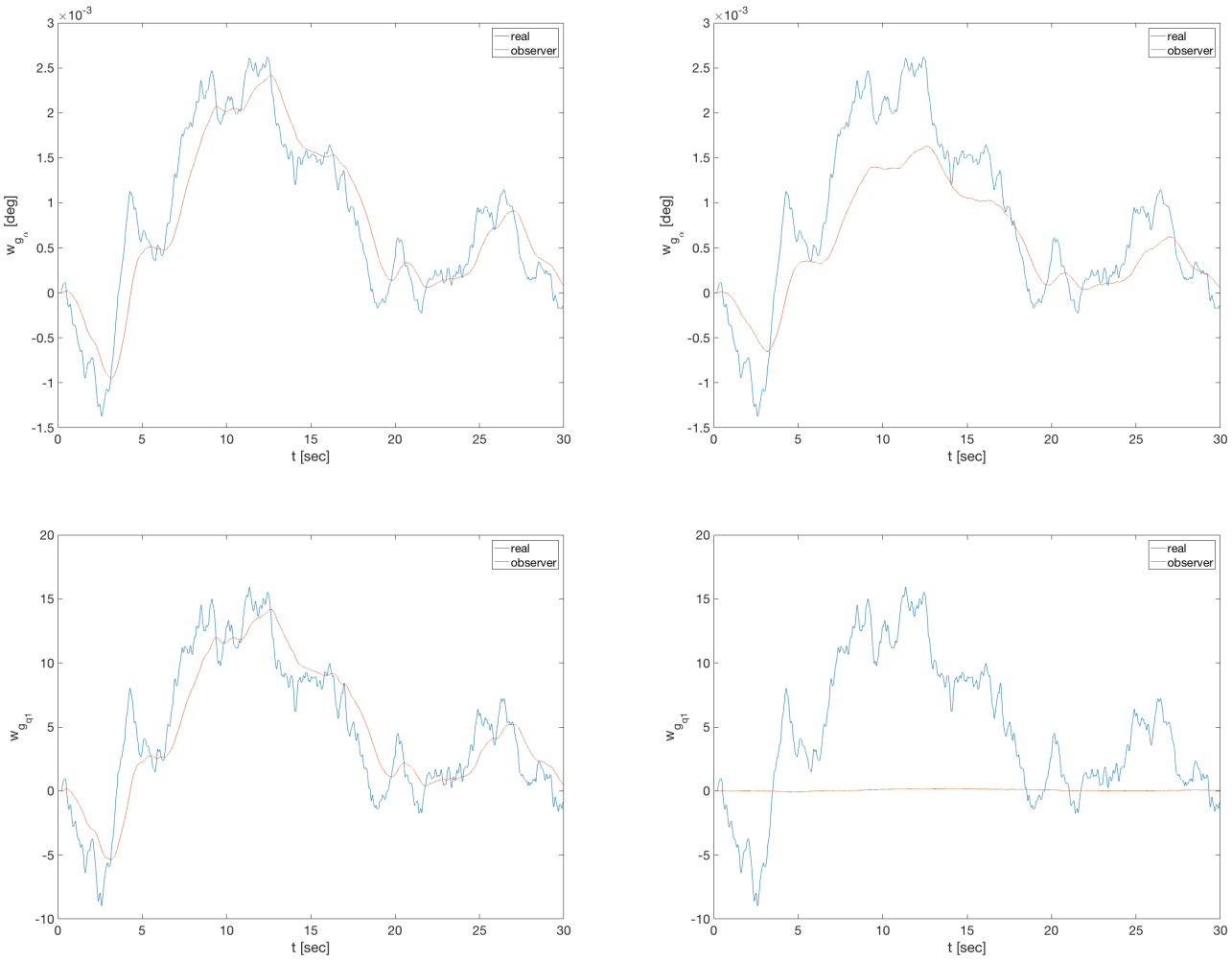

Figure 10. ESO Disturbance Estimation

D. Validation

The active gust load alleviation control is validated for six additional turbulence models.

1. Dryden Light with intensity $\sigma = 1.5$ and characteristic length $L = 1750ft$
2. Dryden Moderate with intensity $\sigma = 1.5$ and characteristic length $L = 1750ft$
3. Dryden Severe with intensity $\sigma = 3.0$ and characteristic length $L = 1750ft$
4. von Kármán Light with intensity $\sigma = 3.0$ and characteristic length $L = 1750ft$

5. von Kármán Moderate with intensity $\sigma = 5.0$ and characteristic length $L = 1750ft$

6. von Kármán Severe with intensity $\sigma = 5.0$ and characteristic length $L = 1750ft$

The validation results are summarized in Table 3. Table 3 shows the difference in performance metrics in percentage when comparing the LQG controller with and without active gust load alleviation. A negative value indicates an increase in performance while a positive values indicates a decrease in performance. For all six turbulence models, active gust load alleviation increases the performance with respect to the rigid-body states $\sum \|x_r - x_{ref,r}\|$, aeroelastic states $\sum \|x_e - x_{ref,e}\|$, and wing root bending moment $M_{y,rms}$. However, it decreases the performance with respect to the flight path angle $\|\gamma - \gamma_{ref}\|$ and does not show any coherent relation with respect to the vertical acceleration at the center of gravity $A_{z,rms}$.

	$\sum \|x_r - x_{ref,r}\|$ [%]	$\sum \|x_e - x_{ref,e}\|$ [%]	$\|\gamma - \gamma_{ref}\|$ [%]	$A_{z,rms}$ [%]	$M_{y,rms}$ [%]
Dryden Light	-21	-17	5	-6	-18
Dryden Moderate	-45	-42	23	2	-43
Dryden Severe	-49	-47	21	-1	-38
von Kármán Light	-31	-40	29	3	-29
von Kármán Moderate	-53	-57	35	1	-59
von Kármán Severe	-38	-43	0	2	-45

Table 3. Validation Results for Active Gust Load Alleviation

V. Discussion

It is important to qualify the limitations and assumptions in this study that may affect the active gust load alleviation assessments.

First, the Kalman filter state estimation needs to be improved in order to improve the performance of the controller and the ESO estimation of the disturbances. The LQR simulation results have indicated the ability of the active gust load alleviation to significantly improve the performance metrics for the rigid-body and aeroelastic responses, wing root bending moment, vertical acceleration of the center of gravity and even the incremental drag. It is expected that the closer the estimation of the aeroelastic states complies with the actual aeroelastic states, the better the LQG controller with active disturbance rejection will perform. Furthermore, the illustration of the ESO disturbance estimation in Fig.10 shows that the ESO disturbance estimation performs very well for the LQR simulations. Following the same line of reasoning, it is expected that a close compliance between the estimates of the aeroelastic states and actual aeroelastic states improves the ESO disturbance estimation for the LQG simulations. A more accurate estimation of the disturbances will improve the active gust load alleviation control.

Secondly, Lyapunov stability theorems are used in general to proof that an MRAC update law is stable. However, in the presence of a bounded disturbance, such as turbulence w_g, only bounded tracking can be accomplished. Furthermore, the robustness of the MRAC update law can be increased by using a robust modification scheme such as optimal control modification.[17,18] Future research should look into the application of the optimal control modification in active gust load alleviation.

Thirdly, this study does not consider any constraints on the rate of the VCCTEF and no lag in the actuator response. Active gust load alleviation requires a highly reactive flap system. In reality, rate constraints and controller lag for the VCCTEF can decrease the performance of the active gust load alleviation control. Future research should study these limitations.

Furthermore, in this study, the VCCTEF is constrained to follow a cubic Chebyshev polynomial shape function. It is plausible that a higher order or more flexible shape function can improve the controller performance by allowing more degrees of freedom. Future research should look into the effect of the shape constraint on the multi-objective flight control and active gust load alleviation control performance.

Finally, stability margins of the controllers should be analyzed to determine how robust they are. This can be done by injecting a time delay at the input to assess the time delay margin of the controllers. The LQR is expected to be most robustly stable among all the controllers but it is not realizable. On the other hand, the LQG design can be designed with a Loop Transfer Recovery (LTR) method to provide a stability margin close to that of the LQR.[16,19]

VI. Conclusions

This paper presents a multi-objective flight control framework for aeroelastic mode suppression, drag minimization, and active gust load alleviation. The present study is an extension of the previous development of multi-objective flight control for flexible aircraft equipped with multi-functional flight control surfaces such as the Variable Camber Continuous Trailing Edge Flap system. The multi-objective flight control addresses multiple competing needs in a flight control design to achieve the goals of maximizing the aerodynamic performance of an aircraft, minimizing structural loads and aeroelastic response of the wing structure, and tracking a pilot command. The aerodynamic performance and structural response objectives are integrated into the traditional cost function of linear-quadratic optimal control to synthesize a multi-objective flight control design. Active gust load alleviation is added to the flight control framework by augmenting the linear-quadratic optimal controller with an adaptive increment. This adaptive increment is designed using Model Reference Adaptive Control and Extended State Observers. The Extended State Observers are used to estimate the turbulence in flight. Simulations of the multi-objective flight control are conducted for a flexible wing NASA Generic Transport Model. The results demonstrate the effectiveness of the active gust

load alleviation approach within a multi-objective flight control framework that includes aeroelastic mode suppression, drag minimization, and gust load alleviation.

Acknowledgements

The authors would like to thank the Fixed Wing / Advanced Air Transport Technology Project under the Advanced Air Vehicles Program of NASA Aeronautics Research Mission Directorate (ARMD) for funding support of this work.

References

[1]Nguyen, N. and Urnes, J., "Aeroelastic Modeling of Elastically Shaped Aircraft Concept via Wing Shaping Control for Drag Reduction," AIAA Atmospheric Flight Mechanics Conference, AIAA-2012-4642, August 2012.

[2]Nguyen, N. and Tal, E., "A Multi-Objective Flight Control Approach for Performance Adaptive Aeroelastic Wing," 56th AIAA/ASCE/AHS/ASC Structures, Structural Dynamics, and Materials Conference (AIAA Science and Technology Forum), January 2015.

[3]Nguyen, N., Ting, E., Chaparro, D., Drew, M., and Swei, S., "Multi-Objective Flight Control for Drag Minimization and Load Alleviation of High-Aspect Ratio Flexible Wing Aircraft," 58th AIAA/ASCE/AHS/ASC Structures, Structural Dynamics, and Materials Conference, AIAA 2017-1589, January 2017.

[4]Nguyen, N., "Elastically Shaped Future Air Vehicle Concept," NASA Innovation Fund Award 2010 Report, October 2010, Submitted to NASA Innovative Partnerships Program, http://ntrs.nasa.gov/archive/nasa/casi.ntrs.nasa.gov/20110023698.pdf.

[5]Nguyen, N., Trinh, K., Reynolds, K., Kless, J., Aftosmis, M., Urnes, J., and Ippolito, C., "Elastically Shaped Wing Optimization and Aircraft Concept for Improved Cruise Efficiency," AIAA Aerospace Sciences Meeting, AIAA-2013-0141, January 2013.

[6]Urnes, J., Nguyen, N., Ippolito, C., Totah, J., Trinh, K., and Ting, E., "A Mission Adaptive Variable Camber Flap Control System to Optimize High Lift and Cruise Lift to Drag Ratios of Future N+3 Transport Aircraft," AIAA Aerospace Sciences Meeting, AIAA-2013-0214, January 2013.

[7]Lebofsky, S., Ting, E., and Nguyen, N., "Aeroelastic Modeling and Drag Optimization of Flexible Wing Aircraft with Variable Camber Continuous Trailing Edge Flap," 32nd AIAA Applied Aerodynamics, AIAA 2014-2443, June 2014.

[8]Ferrier, Y., Nguyen, N., and Ting, E., "Real-time Adaptive Least-Squares Drag Minimization for Performance Adaptive Aeroelastic Wing," 34th AIAA Applied Aerodynamics, AIAA 2016-3567, June 2016.

[9]Nguyen, N., Ting, E., Chaparro, D., Drew, M., and Swei, S., "Multi-Objective Flight Control for Drag Minimization and Load Alleviation of High-Aspect Ratio Flexible Wing Aircraft," 58th AIAA/ASCE/AHS/ASC Structures, Structural Dynamics, and Materials Conference. AIAA 2017-1589, January 2017.

[10]Kaul, U. and Nguyen, N., "Drag Optimization Study of Variable Camber Continuous Trailing Edge Flap (VCCTEF) Using OVERFLOW," 32nd AIAA Applied Aerodynamics, AIAA 2014-2444, June 2014.

[11]Nguyen, N., Ting, E., Nguyen, D., and Trinh, K., "Flight Dynamic Modeling and Stability Analysis of Flexible Wing Generic Transport Aircraft," 55th AIAA/ASME/ASCE/AHS/ASC Structures, Structural Dynamics, and Materials Conference, AIAA-2014-1040, January 2014.

[12]Tal, E. and Nguyen, N., "Unsteady Aeroservoelastic Modeling of Flexible Wing Generic Transport Aircraft with Variable

Camber Continuous Trailing Edge Flap," 33rd AIAA Applied Aerodynamics Conference, AIAA 2015-2722, June 2015.

[13]Tal, E., Nguyen, N. and Ting, E., "Comparison of Unsteady Aerodynamics Approximations for Time-Domain Representation of Frequency-Independent Aeroelastic State-Space Models," 56th AIAA/ASME/ASCE/AHS/ASC Structures, Structural Dynamics, and Materials Conference, January 2015.

[14]Han, J., Control and Decision **138**, Vol. 85, 1995.

[15]Erazo, C., Angulo, F., and Olivar, G., "Stability analysis of the extended state observers by Popov criterion," Theoretical & Applied Mechanics Letters **2**, 043006, 2012.

[16]Lavretsky, E., and Wise, K.A., "Robust and Adaptive Control, with Aerospace Applications," Springer-Verlag, London, 2013, pp. 281-292.

[17]Nguyen, N., Krishnakumar, K., and Boskovic, J., "An Optimal Control Modification to Model-Reference Adaptive Control for Fast Adaptation," AIAA Guidance, Navigation and Control Conference and Exhibit, AIAA 2008-7283, August 2008.

[18]Nguyen, N., "Optimal Control Modification for Robust Adaptive Control with Large Adaptive Gain," Systems & Control Letters, 61 (2012) pp. 485-494.

[19]Stengel, R., "Optimal Control and Estimation," Dover Publications, New York, 1994.

[20]Nguyen, N., Hashemi, K.E., Yucelen, T., and Arabi, E., "Performance Optimizing Multi-Objective Adaptive Control with Time-Varying Reference Model Modification," AIAA Guidance, Navigation, and Control Conference, AIAA-2017-1715, January 2017.

[21]Liu, X., and Sun, Q., "Gust Load Alleviation with Robust Control for a Flexible Wing," Shock and Vibration, Volume 2017, Article ID 1060574, Hindawi Publishing Corporation, November 2015.

[22]Alam, M., Hromcik, M., and Hanis, T., "Active gust load alleviation system for flexible aircraft: Mixed feedforward/feedback approach," Aerospace Science and Technology, 41 (2015) pp. 122-133, Elsevier, December 2014.

[23]Haghighat, S., Liu, H.H.T., and Martins, J.R.R.A., "Model-Predictive Gust Load Alleviation Controller for a Highly Flexible Aircraft," Journal of Guidance, Control, and Dynamics, Vol. 35, No.6, November-December 2012.

[24]Frost, S.A., Taylor, B.R., and Bodson, M., "Investigation of Optimal Control Allocation for Gust Load Alleviation in Flight Control," AIAA Atmospheric Flight Mechanics Conference, AIAA 2012-4858, August 2012.

[25]Huang, Y., Xu, K., Han, J., and Lam, J., Flight Control Design using Extended State Observer and Non- Smooth Feedback, 40th IEEE Conference on Decision and Control, 2001.

[26]Drela, M., and Youngren, H., AVL 3.26 User Primer, MIT Aero/Astro, Aerocraft, Inc., Cambridge, MA, 2006.

[27]Theodorsen, T., "General Theory of Aerodynamic Instability and the Mechanism of Flutter," NACA-TR-496, January 1949.

[28]Basappa and Jategaonkar, R.V., "Evaluation of Recursive Methods for Aircraft Parameter Estimation," AIAA Atmospheric Flight Mechanics Conference and Exhibit, AIAA 2004-5063, August 2004.

[29]Su, W., Reich, G., "Modeling of Artificial Hair Sensors for Vibration Control of Flexible Wings," AIAA/ASCE/AHS/ASC Structures, Structural Dynamics, and Materials Conference, AIAA-2016-1958, January 2016.

[30]Boeing Report No. 2012X0015, "Development of Variable Camber Continuous Trailing Edge Flap System," October 4, 2012.

[31]Nguyen, N, Precup, N., Urnes, J., Nelson, C., Lebofsky, S., Ting, E., and Livne, E., "Experimental Investigation of a Flexible Wing with a Variable Camber Continuous Trailing Edge Flap Design," 32nd AIAA Applied Aerodynamics Conference, AIAA-2014-2442, June 2014.

[32]Nguyen, N., Ting, E., Nguyen, D., Trinh, K., "Flutter Analysis of Mission-Adaptive Wing with Variable Camber Contin-

uous Trailing Edge Flap," 55th AIAA/ASME/ASCE/AHS/ASC Structures, Structural Dynamics, and Materials Conference, AIAA-2014-0839, January 2014.

[33]Nguyen, N., Swei, S., and Ting, E., "Adaptive Linear Quadratic Gaussian Optimal Control Modification for Flutter Suppression of Adaptive Wing," AIAA Infotech@Aerospace Conference, AIAA 2015-0118, January 2015.

[34]Kokotovic, P., Khalil, H., and O'Reilly, J., *Singular Perturbation Methods in Control: Analysis and Design*, Society for Industrial and Applied Mathematics, 1987.

[35]Ardema, M., "Computational Singular Perturbation Method for Dynamical Systems", AIAA Journal of Guidance, Control, and Dynamics, Vol. 14, pp. 661-663, 1981.

[36]Ippolito C. and Nguyen, N., "A Preliminary Study for Optimal Longitudinal-Mode Flight Control through Distributed Aeroelastic Shaping," 55th AIAA/ASME/ASCE/AHS/ASC Structures, Structural Dynamics, and Materials Conference, AIAA-2014-1044, January 2014.

[37]Brown, N. and Schaefer, J., "Peak-Seeking Optimization of Trim for Reduced Fuel Consumption: Flight-Test Results," AIAA Guidance, Navigation, and Control Conference, AIAA-2013-5171, August 2013.

[38]Nobbs, S.G., "Development of the Full-Envelope Performance Seeking Control Algorithm," 28th AIAA Joint Propulsion Conference, AIAA-1992-3748, July 1992.

A. Optimal Disturbance Gain

This appendix shows the derivation of the optimal disturbance gain K_w. Consider our system

$$\dot{x} = Ax + Bu + z + w_g \tag{91}$$

An optimal control is designed with the following cost function

$$J = \frac{1}{2}\int_0^{t_f} \left(x^T Q x + u^T R u\right) dt \tag{92}$$

where $Q = Q_r \oplus Q_e \oplus Q_\delta \oplus Q_s \oplus Q_a > 0$.

We define the Hamiltonian as

$$H = \frac{1}{2}\left(x^T Q x + u^T R u\right) + \lambda^T \left(Ax + Bu + z + w_g\right) \tag{93}$$

The adjoint equation and optimal control are obtained as

$$\dot{\lambda} = -\frac{\partial H^T}{\partial x} = -Qx - A^T\lambda \tag{94}$$

$$\frac{\partial H^T}{\partial u} = Ru + B^T\lambda = 0 \Rightarrow u = -R^{-1}B^T\lambda \tag{95}$$

Let $\lambda = Wx + Vz + T$. Then

$$\dot{W}x + W\dot{x} + \dot{V}z + V\dot{z} + \dot{T} = -Qx - A^T\left(Wx + Vz + T\right) \tag{96}$$

In this study, the command flight path angle γ_c is constant and therefore $\dot{\gamma}_c = 0$. Let $t_f \to \infty$, then the optimal solution approaches a steady state solution. For the infinite time-horizon optimal control, $\dot{W}\left(t_f\right) = 0$, $\dot{V}\left(t_f\right) = 0$, and $T\left(t_f\right) = 0$. Then, separating terms yields the following expressions

$$WA + A^T W - WBR^{-1}B^T W + Q = 0 \tag{97}$$

$$V = -\left(A^T - WBR^{-1}B^T\right)^{-1} W \tag{98}$$

$$\dot{T} = -\left(A^T - WBR^{-1}B^T\right) T - Ww_g \tag{99}$$

For control implementation, Eq.(99) needs to be calculated numerically. The real disturbance w_g is replaced with the observed disturbance $\hat{w}_g$. Equation 99 becomes

$$\dot{T} = -\left(A^T - WBR^{-1}B^T\right)T - W\hat{w}_g \tag{100}$$

Since the transversality condition is based on the terminal time condition, a time-to-go variable τ is defined as

$$\tau = t_f - t \tag{101}$$

Numerically solving Eq.(99) as function of the time-to-go variable τ gives

$$\dot{T} = \frac{T_{i+1} - T_i}{\Delta\tau} = -\left(A^T - WBR^{-1}B^T\right)T - W\hat{w}_g \tag{102}$$

$$T_{i+1} = T_i - \Delta\tau\left(\left(A^T - WBR^{-1}B^T\right)T - W\hat{w}_g\right) \tag{103}$$

The differential equation from Eq.(103) cannot be implemented in real-time. For infinite time-horizon control, as $\tau \to 0$, the optimal control solution will approach a steady-state solution that consists of infinite series containing the time derivatives of the observed disturbance $\hat{\dot{w}}_g$.

Another approach would be to define λ as $\lambda = Wx + Vz + Tw_g$. The adjoint equation in Eq.94 then becomes

$$\dot{W}x + W\dot{x} + \dot{V}z + V\dot{z} + \dot{T}w_g + T\dot{w}_g = -Qx - A^T\left(Wx + Vz + Tw_g\right) \tag{104}$$

It is invalid to assume that $\dot{w}_g = 0$ and therefore Eq.(104) cannot be solved analytically nor numerically. The time derivatives of the disturbance $\dot{w}_g$ could be estimated using the ESO gust estimation update law from Eq.(64). However, Eq.(104) can still not be implemented because T depends on the time derivatives of the disturbance $\dot{w}_g$ and the estimates of the time derivatives of the disturbance $\hat{\dot{w}}_g$ are time-varying.

Nonetheless, sub-optimal solutions are usually adequate by neglecting $\hat{\dot{w}}_g$. Then upon setting $\dot{W}\left(t_f\right) = 0$, $\dot{V}\left(t_f\right) = 0$, and $T\left(t_f\right) = 0$ for the infinite time-horizon solution and substituting the definition of $\dot{x}$ from Eq.(91) into the adjoint equation from Eq.(104) gives

$$W\left(Ax + Bu + z + w_g\right) = -Qx - A^T\left(Wx + Vz + Tw_g\right) \tag{105}$$

Separating terms yields the following expressions

$$WA + A^T W - WBR^{-1}B^T W + Q = 0 \tag{106}$$

$$V = -\left(A^T - WBR^{-1}B^T\right)^{-1} W \tag{107}$$

$$T = -\left(A^T - WBR^{-1}B^T\right)^{-1} W \tag{108}$$

In the presence of state and disturbance estimation, the multi-objective flight controller is expressed as

$$u = K_x \hat{x} + K_z z + K_w \hat{w}_g \tag{109}$$

where

$$K_x = -R^{-1}B^T W \tag{110}$$

$$K_z = -R^{-1}B^T V \tag{111}$$

$$K_w = -R^{-1}B^T T \tag{112}$$